Scientific Reports

ARTICLE | Article in Press

Nonlinear wave dynamics and structural response of hybrid nanocomposite open shells under aerodynamic forces on a friction-coupled elastic foundation

Hamed Safarpour · Loke Kok Foong · Murat Yaylacı · Mustafa Bayram

Received: 8 January 2026 / Accepted: 11 September 2026
© The Author(s) 2026

Abstract

It is extremely important to have information about the stability and wave propagation characteristics of the aircraft structure due to high-speed aerodynamic loads in order to design the next generation of flight vehicles. In this research work, a new coupled methodology between aerodynamics and foundation for nonlinear dispersion of a doubly curved nanocomposite fuselage panel in a supersonic flow regime is proposed. The material is made of an epoxy-based matrix reinforced by nanocrystalline alumina and is resting on a viscoelastic foundation with consideration of all possible interaction forces. Unlike the traditional aeroelastic theory, the proposed methodology offers a physically sound modification to the classical first-order supersonic piston theory. As a result, the aerodynamic loading is state-dependent and inherently dependent on the supporting medium, and the model naturally reduces to classical piston theory in the absence of any foundation effects. The deformation kinematics of the structure are formulated based on higher-order shear deformation theory having a hyperbolic shear strain distribution, while the geometric nonlinearity in the model has been accounted for by means of von Kármán strain-displacement relations. Hamilton's principle is utilized to develop the fully coupled nonlinear governing equations, and these governing equations have been validated by making extensive comparisons with published results as well as by a separate finite element formulation. The system of nonlinear algebraic equations obtained from the governing equations is solved using the harmonic balance method to determine dispersion characteristics along with nonlinear group and phase velocities. Extensive parametric studies show that the proposed fully coupled aeroelastic model is capable of predicting very complicated instability characteristics, flutter boundaries, wave propagation characteristics, and dispersion properties that cannot be captured by traditional uncoupled models.

Keywords Aeroelastic stability · Nonlinear dynamics · Wave dispersion · Group and phase velocity · Supersonic piston theory · Doubly curved panels.

This Article in Press is shared early to give you faster access to new research. It is citable and carries a permanent DOI. The final edited version will replace it automatically.



https://doi.org/10.1038/s41598-026-71917-0

Published online: 27 September 2026

scientific reports

Introduction

Reinforcement of composites by the use of nano-fillers has proved to be a revolution in materials engineering[1]. This is extremely crucial in the sense that even small amounts of nano-particles like layered silicates, carbon nanotubes, or graphene can result in great improvement in mechanical properties[2]. The difference from traditional filler reinforcements lies in the fact that nano-filler reinforcements have an exceptionally large surface area to volume ratio, hence improving adhesion and stress transfer between the reinforcement and the matrix[3]. It has been found that nanocomposites possess great tensile strength and elastic modulus in addition to fracture toughness compared to other composites[4]. Besides, nano-scale dispersion of reinforcement phases prevents crack formation and propagation[5]. In addition to their excellent mechanical properties, the reinforcement of composites at the nano-scale greatly increases their thermal stability and flame-retardant ability, rendering them applicable for use in high-temperature environments of the aerospace and automotive industries[6]. Electrical conductivity of normally non-conducting polymeric matrices could be achieved by means of incorporating electrically conductive nanoparticles, like carbon nanotubes or graphene[7]. Another effect that might be mentioned is that of a nucleating agent on the morphology and performance of the polymer matrix due to the presence of nanofillers[8]. These combined multifunctional properties make it possible to create lightweight and high-performing materials, decreasing energy consumption and extending the life span of the components[9].

Stability analysis is an essential field of study in aerospace engineering, which ensures that the construction of aircraft and spacecraft sustains its desired load distribution capacity without suffering from any failure or collapse[10]. In contrast to static strength analysis, stability analysis focuses on sudden and unexpected changes in geometry or dynamics that occur well before reaching the yield stress of the material[11]. Some of the most prevalent types of stability problems encountered in thin-walled aerospace structures are buckling, post-buckling, divergence, and flutter, each having its unique physical phenomena[12]. For example, buckling is an abrupt deflection of relatively small structures subjected to either compressive or shear stress[13], while flutter is an unstable aeroelastic behavior caused by the interaction between aerodynamic, elastic, and inertial forces leading to destructive oscillations[14]. It should be noted that, due to the lightweight and high strength of contemporary aerospace structures, they are more prone to stability problems under extreme flight conditions[15]. Stability analysis methodologies include linear buckling analysis through eigenvalues, nonlinear buckling through post-buckling analysis, as well as finite element analyses that have the capability to detect geometric imperfections and material nonlinearity[16]. Flutter boundary determination as well as preventing resonance at high speeds requires modal analysis and Computational Fluid Structure Interaction analysis[17]. Regulatory bodies require comprehensive stability analyses on primary structures such as wing structures, fuselage, and control surfaces[18]. Stability analysis not only helps in ensuring that catastrophic failure is prevented, but it also assists in designing optimum and lightweight structures which are important for performance and mission success[19].

Computer simulation has become an integral part of science and engineering today, allowing the creation of virtual representations of physical phenomena that are either too costly, hazardous, or difficult to perform by simulation[20,21]. In contrast to conventional analytical models, which are only applicable for simple shapes and linear systems, computer simulations enable dealing with complicated, nonlinear, and multiphysics problems with a high degree of accuracy[22,23]. This feature makes it possible for scientists and engineers to analyze a broad range of designs, performing numerous iterations with different sets of parameters without building any physical prototypes[24,25]. In addition, by modeling the system's performance at high loadings, in corrosive media, or other nonstandard conditions, computer simulations decrease the need for expensive and lengthy physical experimentation[26,27]. Moreover, computer simulations make it possible to obtain data on the internal variables and fields, such as stress distribution, flow velocity, or electromagnetic field, which cannot be measured experimentally[28,29].

Computer simulation in structural analysis allows for the assessment of failure modes, fatigue life, and stability limitations way before any real structure has been constructed[30,31]. In cases of safety-critical industries, such as the aerospace industry, automotive industry, and nuclear engineering, simulations provide proof for certification

and compliance with regulations, without putting people's lives in danger by showing the worst-case scenarios that could happen[32,33]. Simulations also help with uncertainty analysis and sensitivity analysis by making it possible to understand which design variables have a larger impact on the performance/reliability[34,35]. With the combination of simulation techniques with optimization and machine learning techniques, innovation in lightweight, energy-efficient, and high-performance structures is sped up[36,37]. In conclusion, computer simulation not only results in a reduction of product development times and costs, but also allows for innovation that would not have been possible without the use of either experimentation or theory alone[38].

The shell structures are used extensively in various engineering applications due to their efficient structural performance and lightweight properties. Shell structures are an integral part of aircraft and spacecraft construction as they ensure a high strength-to-weight ratio and good dynamic performance of the structure[39]. The use of the shell model in nanomechanics allows precise analysis of the deformation and vibration modes of biological objects, such as viruses, under the influence of various loads[40]. Shell structures can also find application in biomedicine, where the mathematical models of shell structures can be used for the analysis of the mechanical behavior of human organs and the study of the related pathologies[41]. The cylindrical and toroidal shell structures have particular importance in the sphere of space systems engineering as they provide good structural solutions suitable for advanced space environments and artificial gravity designs[42]. The development of advanced shell theories for composite and functionally graded materials makes it possible to design multifunctional structures with optimal performance and materials distribution[43]. Spherical and conical shell structures find wide applications in modern engineering due to their capability to withstand various loads and improve the performance of advanced structural systems[44,45].

Wave propagation in advanced composites and metamaterials has become an area of interest in recent times. In this context, Gao et al.[46] have studied the manipulation of flexural waves in perforated metamaterial plates consisting of acoustic black holes connected through piezoelectric studs. It was observed that the properties of the bandgap could be controlled actively. In addition, Gao et al.[47] carried out a study on wave propagation in smart sandwich plates, comprising functionally graded nanocomposite porous material with piezoelectric layers. The effects of porosity and electromechanical fields on dispersion curves were discussed in detail. Gao et al.[48] have also studied the effect of graphene platelet dispersion and porosity on wave propagation in functionally graded porous plates. In these studies, only linear wave propagation is considered in flat or sandwich plates. However, in the current study, wave dispersion in nonlinear aeroelastic waves in doubly curved nanocomposite shells with coupled aerodynamic foundation interaction is considered.

To the best of the authors' knowledge, all previous literature on supersonic aeroelasticity of composite shells considered only the aerodynamic pressure and the elastic foundation. The critical limitation addressed in the current study is that all previous nonlinear wave equations in the field of aeroelasticity considered the supersonic aerodynamic pressure and elastic foundation as independent parameters, thereby disregarding the fact that the stiffening effect of the foundation inherently influences the aerodynamic pressure field. As a result, dispersion and flutter boundary predictions for such systems become highly inaccurate, especially at the short wavelength range when the influence of the foundation becomes significant. To address this important research gap, this paper proposes a novel mathematical modeling approach that couples the first-order supersonic piston theory with multi-parameter Winkler-Pasternak properties of the elastic foundation. Through formulating a state-dependent aerodynamic problem, the stiffness properties of the foundation inherently influence the convective aeroelastic pressure, thereby participating in the process of wave propagation. Moreover, the proposed higher-order shear deformation theory considers Von Karman nonlinearities to simulate large deformations of hybrid nanocrystalline alumina-reinforced doubly curved fuselage panels.

In order to achieve the highest possible level of physical and mathematical consistency, the coupled equations that have been developed are verified in full against analytical standards and also independent FEM solutions generated during this study. Finally, harmonic balance is utilized for detailed analysis of the coupled influences of structural curvature, nano-reinforcement distribution, and the influence of the foundation and aerodynamics on the nonlinear velocity landscapes. In order to clearly specify the novelty in the current investigation, three key

aspects are highlighted. First, the coupling of physically consistent nature between the supersonic flow pressure and multi-parameter elastic foundation has been proposed through the state-dependent interaction coefficient, which inherently modifies the convection pressure term – an effect missing from all other uncoupled approaches. Second, it is the first approach that considers the nonlinear (quadratic and cubic) foundation stiffness, frictional sliding, and torsional resistance in a hyperbolic higher-order shear deformation theory of doubly-curved nanocomposite shells. Third, in contrast to other research efforts which only consider the linear frequency or a single velocity parameter, the current analysis provides both nonlinear phase and group velocities through a high-order harmonic balance technique in this fully coupled aeroelastic system.

Effective material properties

Material properties formulations of nano-alumina

The incorporation of nano-alumina particles into polymer, metallic, or ceramic matrices has gained considerable attention due to their high stiffness, thermal stability, and wear resistance. Accurately formulating the effective material properties of nano-alumina-reinforced composites is essential for predicting mechanical behavior and optimizing structural performance. Following the established synthesis protocols in Refs[49,50]., the effective mechanical properties of the nano-alumina/epoxy composite are obtained as follows.

Nano-alumina is selected for its high elastic modulus (350 GPa), low density, and superior stiffness-to-weight ratio, critical for supersonic aeroelastic stability. The different distribution patterns of the presented nanocomposite reinforcement can be formulated as follows:

$$\text{Pattern X}: \; V^{A}_{nAl_2O_3}(\mathcal{Z}) = \frac{4|\mathcal{Z}|}{h} V^{T}_{nAl_2O_3} \tag{1}$$

$$\text{Pattern O}: \; V^{O}_{nAl_2O_3}(\mathcal{Z}) = \left(2 - \frac{4|\mathcal{Z}|}{h}\right) V^{T}_{nAl_2O_3} \tag{2}$$

$$\text{Pattern V}: \; V^{V}_{nAl_2O_3}(\mathcal{Z}) = \left(\frac{\mathcal{Z}}{h} + 0.5\right) 2V^{T}_{nAl_2O_3} \tag{3}$$

$$\text{Pattern UD}: \; V^{UD}_{nAl_2O_3}(\mathcal{Z}) = V^{T}_{nAl_2O_3} \tag{4}$$

$$\text{Pattern A}: \; V^{X}_{nAl_2O_3}(\mathcal{Z}) = \left(1 - \frac{\mathcal{Z}}{h}\right) V^{T}_{nAl_2O_3} \tag{5}$$

The five distribution patterns (X, O, V, UD, and A) are standard parametric representations of through-thickness reinforcement gradients, extensively used in functionally graded material modeling to mimic various manufacturing-induced segregation phenomena, such as gravity settling, surface enrichment, or uniform dispersion. These canonical forms allow systematic investigation of grading effects without loss of generality[51]. The volume fraction of nAl_2O_3 can be formulated as follows:

$$V^{T}_{nAl_2O_3} = \frac{W_{nAl_2O_3}}{W_{nAl_2O_3} + (\rho_{nAl_2O_3}/\rho_{M})(1 - W_{nAl_2O_3})}. \tag{6}$$

In this equation, the symbol $W_{nAl_2O_3}$ denotes the weight fraction of the nanocomposite reinforcement. The geometry factor encapsulates both the form and the relative amount of nano-alumina particles, which significantly influence how much mechanical reinforcement they provide. This factor is calculated as the ratio of a particle's diameter to its thickness.

$$\xi_l = \xi_t = \frac{2d_{nAl_2O_3}}{h_{nAl_2O_3}} \tag{7}$$

The effectiveness of reinforcement, driven by the stiffness contrast between the matrix material and the nano-alumina, is captured by these factors. The magnitude of these factors is governed not only by the shape of the particles but also by their mechanical properties.

$$\eta_l = \frac{\left(\frac{E_{nAl_2O_3}}{E_M} - 1\right)}{\left(\frac{E_{nAl_2O_3}}{E_M} + \xi_l\right)}, \tag{8}$$

$$\eta_t = \frac{\left(\frac{E_{nAl_2O_3}}{E_M} - 1\right)}{\left(\frac{E_{nAl_2O_3}}{E_M} + \xi_t\right)}. \tag{9}$$

The nanocomposite's stiffness along the longitudinal axis (E_l) and the transverse axis (E_t) is calculated using the two equations below. These equations incorporate three key factors: the concentration of particles, their geometry, and the quality of interfacial interaction between the particles and the matrix material.

$$E_{nAl_2O_3} = 0.49E_l + 0.51E_t, \tag{10}$$

$$E_l = \frac{E_M(1 + \xi_l \eta_l V_{nAl_2O_3})}{1 - \eta_l V_{nAl_2O_3}}, \tag{11}$$

$$E_t = \frac{E_M(1 + \xi_t \eta_t V_{nAl_2O_3})}{1 - \eta_t V_{nAl_2O_3}}. \tag{12}$$

The coefficients 0.49 and 0.51 are empirical weighting factors derived from the Halpin-Tsai averaging scheme for randomly oriented nano-alumina particles, representing the volumetric contribution of longitudinal and transverse stiffness, respectively. These specific values are taken from the experimental curve-fitting calibration reported in Refs[52,53] for the Al_2O_2/epoxy system. The Poisson's ratio of the composite is approximated as follows.

$$\upsilon_{nAl_2O_3} = \upsilon_M V_M + \upsilon_{nAl_2O_3} V_{nAl_2O_3}, \tag{13}$$

Using a volume-fraction-based rule of mixtures, the Poisson's ratio of the composite is approximated, which describes how the material deforms in directions orthogonal to the direction of the applied force.

$$\rho_{nAl_2O_3} = \rho_M V_M + \rho_{nAl_2O_3} V_{nAl_2O_3}, \tag{14}$$

Similar to the approach used for Poisson's ratio, the overall density of the composite is derived from the densities and volumetric fractions of each component. This property plays a key role in both structural assessment and dynamic simulation.

$$V_{nAl_2O_3} + V_M = 1. \tag{15}$$

This requirement ensures the preservation of volume by assuming that the composite contains only the matrix and the reinforcing phases. This assumption forms the essential basis upon which the validity of all the following equations rests. Table 1[52,53] presents the properties of the epoxy-based structure reinforced with nano-alumina.

It is assumed that the synthesis protocol (ultrasonic deagglomeration and mechanical mixing) achieves uniform dispersion and perfect interfacial bonding, as validated in Refs[49,50]. Under this ideal condition, the effective elastic properties depend exclusively on the intrinsic moduli of the neat constituents (Table 1) and their volume fractions, rendering the use of these literature-based material parameters consistent with the present macroscopic modeling.

Table 1 The material properties of the epoxy structure reinforced by nAl2O3.

Material	Elasticity modulus (GPa)	Mass density (kg/m³)	Poisson's ratio
nAl_2O_3			
Epoxy	30	2300	0.2
Nano-Alumina	350	3900	0.22

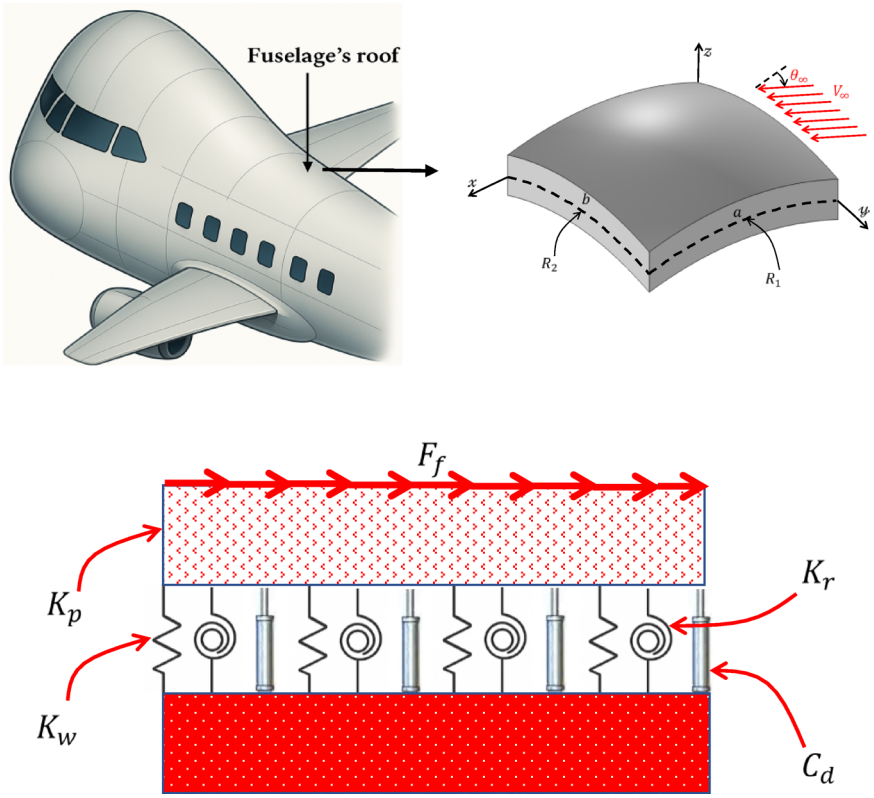


Fig. 1 Key components of an aircraft fuselage panel resting on a multi-parameter elastic foundation.

Mathematical modeling

Figure 1 illustrates the key components of an aircraft fuselage panel resting on a multi-parameter elastic foundation. The panel, representing a section of the fuselage roof, is subjected to a combination of foundation reactions. K_w and K_p denote the Winkler and Pasternak elastic moduli, respectively, which provide normal and shear resistance. A frictional force F_f opposes relative motion at the interface, while C_d represents the damping coefficient of the viscoelastic foundation, dissipating vibrational energy. The radii R_1 and R_2 indicate the double curvature of the panel, characteristic of aircraft fuselage geometry. Additionally, K_r corresponds to the torsional foundation coefficient, accounting for rotational stiffness. Together, these parameters form a comprehensive mechanical model that includes elastic, damping, frictional, and torsional effects. Such a representation is essential for accurately predicting the aeroelastic response, wave propagation, and flutter behavior of nano-alumina-reinforced fuselage panels under supersonic airflow and foundation interaction.

Mathematical formulations

Displacement field

Following the HSDT, a generic displacement field involving five variables (u, v, w) can be expressed for any arbitrary patch as follows:

$$u(x,y,z,t) = u_0(x,y,t) - z\frac{\partial w_0(x,y,t)}{\partial x} + f(z)\theta_x(x,y,t), \tag{16}$$

$$v(x,y,z,t) = v_0(x,y,t) - z\frac{\partial w_0(x,y,t)}{\partial y} + f(z)\theta_y(x,y,t), \tag{17}$$

$$w(x,y,z,t) = w_0(x,y,t). \tag{18}$$

In this expression, the mid-plane displacement components along the x, y, and z axes are denoted by (u_0, v_0, w_0), while (θ_x, θ_y) represent the rotations within the xz and yz planes, respectively. The variable t indicates time, and $f(z)$ refers to the shape function, which is taken to be of a hyperbolic form according to Ref.[54].

$$f(z) = \frac{\frac{h}{\pi}sinh\left(\frac{\pi}{h}z\right) - z}{\left[cosh\left(\frac{\pi}{2}\right) - 1\right]}. \tag{19}$$

Selection of HSDT with hyperbolic function for transverse shear deformation in preference to the other kinematic models hinges on three major factors. First, in contrast to FSDT, which assumes constant transverse shear strains across the cross section and thus necessitates an empirical shear correction factor that varies depending on material, boundaries, and loadings, the HSDT fulfills zero transverse shear stress conditions at the top and bottom surfaces without any shear correction factor, ensuring the physical nature[55]. Second, for the current nano-alumina/epoxy composite material with a high face-to-core stiffness ratio, transverse shear deformations play a crucial role, especially for the short-wavelength range associated with wave propagation; the hyperbolic function describes parabolic behavior of the shear strains with high accuracy, whereas FSDT would underestimate the above effects. Third, although the CUF provides a broad scheme for formulating arbitrary-order theories, it needs convergence analysis with respect to the expansion order[56]. The hyperbolic HSDT formulation offers an optimally balanced accuracy-efficiency trade-off in that it obtains the same level of accuracy as higher-order CUF theories using five unknowns, which is vital for the present non-linear aeroelasticity study where harmonic balance iterations have to be done repeatedly (Figs. 2, 3, 4, 5 and 6).

Constitutive relations

The relationship between displacement and strain is derived by including Von Kármán's geometric nonlinearities, which are tailored to doubly curved shallow shell structures[51].

$$\left\{\begin{array}{c}\varepsilon_x\\ \varepsilon_y\\ \gamma_{xy}\end{array}\right\} = \left\{\begin{array}{c}\frac{\partial u}{\partial x} - \frac{w}{R_x} + \frac{1}{2}\left(\frac{\partial w}{\partial x}\right)^2\\ \frac{\partial v}{\partial y} - \frac{w}{R_y} + \frac{1}{2}\left(\frac{\partial w}{\partial y}\right)^2\\ \frac{\partial u}{\partial y} + \frac{\partial v}{\partial x} + \frac{\partial w}{\partial x}\frac{\partial w}{\partial y}\end{array}\right\}, \quad \left\{\begin{array}{c}\gamma_{xz}\\ \gamma_{yz}\end{array}\right\} = \left\{\begin{array}{c}\frac{\partial u}{\partial z} + \frac{\partial w}{\partial x}\\ \frac{\partial v}{\partial z} + \frac{\partial w}{\partial y}\end{array}\right\}. \tag{20}$$

Inserting Eq. (9) into Eq. (11) gives:

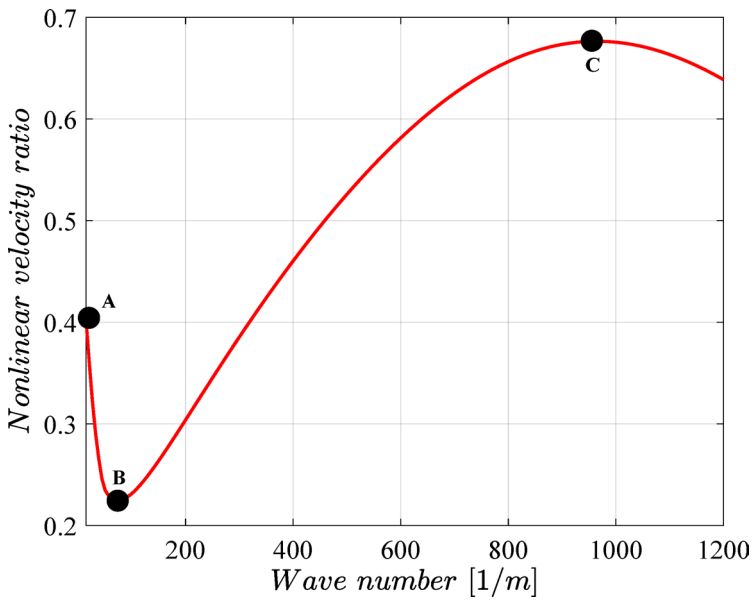
$$\mathcal{E} = \mathcal{E}^0 + zk^1 + f(z)k^3, \tag{21}$$

Algorithm 1: Iterative harmonic balance for nonlinear group/phase velocity Input: panel parameters, foundation coefficients, aerodynamic λ, initial amplitude A^*, wave number k Output: $\omega(\mathrm{t})$, NPV, NGV.

1. Compute linear stiffness matrices and mass inertias (Eqs. 20a-e)
2. Assemble and solve linearized Eqs. (36a-e) to obtain initial $\mathbb{C}$, γ_{11}, γ_{12}, γ_{13}
3. Set initial guess: $\mathbb{A}_1 = A^*/h, \mathbb{A}_0 = \mathbb{A}_2 = \mathbb{A}_3 = \mathbb{A}_4 = \mathbb{A}_5 = \mathbb{A}_6 = 0$
4. Repeat until convergence (max relative change < 1e-8):
5. Compute $\mathbb{L}_{\mathbb{B}1}$, $\mathbb{L}_{\mathbb{B}2}$ using Eqs. (41a-u) with current $\mathbb{A}_{\mathbb{B}}$
6. Update $\mathbb{A}_{\mathbb{B}}$ ($\mathbb{B} = 0,2,3,4,5,6$) using Eq. (42)
7. Update $\mathbb{A}_1$ from the $\mathbb{B} = 1$ equation (implicitly satisfied)
8. End repeat
9. Compute $\omega(\mathrm{t})$ from Eq. (45a) using numerical integration (trapezoidal rule)
10. Compute $NPV = \omega/k$, $NGV = d\omega/dk$ (central finite difference)

Fig. 2 The Pseudocode of the harmonic balance solution.

Fig. 3 Nonlinear velocity ratio as a function of the wave number.



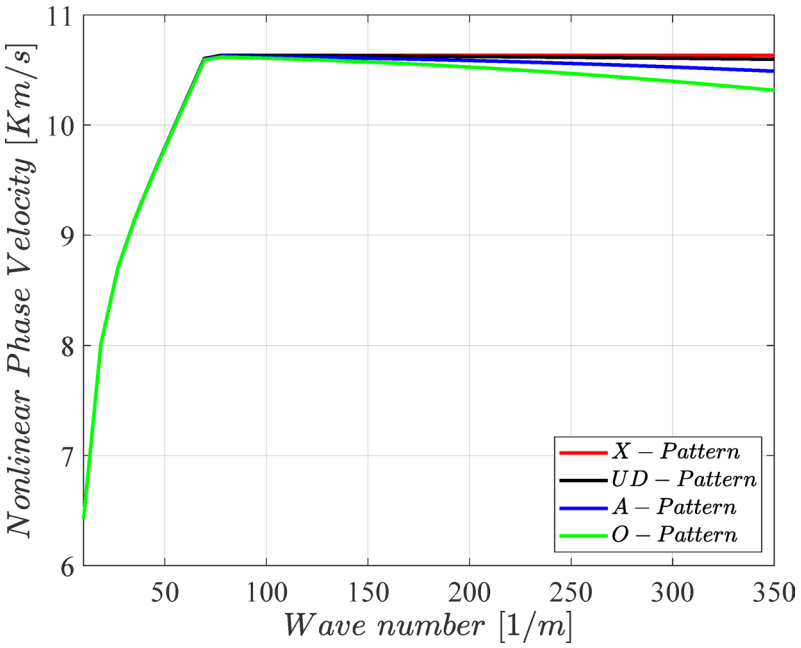


Fig. 4 The influence of different nano-alumina distribution patterns on the NPV as a function of wave number.

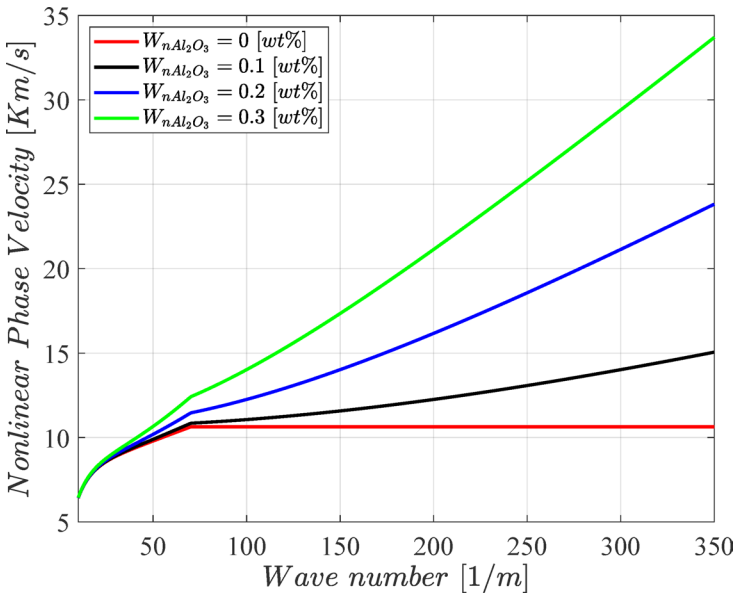


Fig. 5 The influence of different nano-alumina weight fractions on the NPV as a function of wave number.

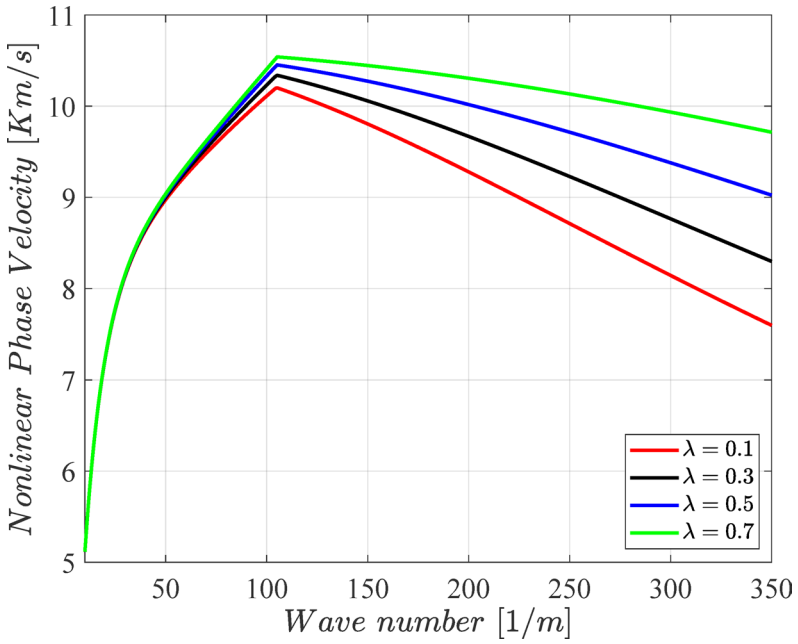


Fig. 6 The variation of the NPV as a function of wave number for different values of the non-dimensional aerodynamic pressure parameter.

$$\gamma = \mathbb{g}(z)k^2. \tag{22}$$

where

$$\mathcal{E}^0 = \left\{ \begin{array}{c} \mathcal{E}_x^0 \\ \mathcal{E}_y^0 \\ \gamma_{xy}^0 \end{array} \right\} = \left\{ \begin{array}{c} \frac{\partial w_0}{\partial x} - \frac{w_0}{R_x} + \frac{1}{2}\left(\frac{\partial w_0}{\partial x}\right)^2 \\ \frac{\partial w_0}{\partial y} - \frac{w_0}{R_y} + \frac{1}{2}\left(\frac{\partial w_0}{\partial y}\right)^2 \\ \frac{\partial w_0}{\partial y} + \frac{\partial w_0}{\partial x} + \frac{\partial w_0}{\partial x}\frac{\partial w_0}{\partial y} \end{array} \right\}, \tag{23}$$

$$k^1 = \left\{ \begin{array}{c} k_x^1 \\ k_y^1 \\ k_{xy}^1 \end{array} \right\} = \left\{ \begin{array}{c} -\frac{\partial^2 w_0}{\partial x^2} \\ -\frac{\partial^2 w_0}{\partial y^2} \\ -2\frac{\partial^2 w_0}{\partial x \partial y} \end{array} \right\}, \; k^2 = \left\{ \begin{array}{c} k_{xz}^2 \\ k_{yz}^2 \end{array} \right\} = \left\{ \begin{array}{c} \theta_x \\ \theta_y \end{array} \right\}, \; \mathbb{g}(z) = \frac{\mathrm{d}f(z)}{\mathrm{d}z}, \tag{24}$$

$$k^3 = \left\{ \begin{array}{c} k_x^3 \\ k_y^3 \\ k_{xy}^3 \end{array} \right\} = \left\{ \begin{array}{c} \frac{\partial \theta_x}{\partial x} \\ \frac{\partial \theta_y}{\partial y} \\ \frac{\partial \theta_x}{\partial y} + \frac{\partial \theta_y}{\partial x} \end{array} \right\}. \tag{25}$$

The stress-strain relationships for the composite panel are expressed as follows:

$$\left\{ \begin{array}{c} \sigma_x \\ \sigma_y \\ \sigma_{xy} \\ \sigma_{yz} \\ \sigma_{xz} \end{array} \right\} = \left\{ \begin{array}{ccccc} \mathfrak{M}_{11} & \mathfrak{M}_{12} & 0 & 0 & 0 \\ \mathfrak{M}_{12} & \mathfrak{M}_{22} & 0 & 0 & 0 \\ 0 & 0 & \mathfrak{M}_{66} & 0 & 0 \\ 0 & 0 & 0 & \mathfrak{M}_{44} & 0 \\ 0 & 0 & 0 & 0 & \mathfrak{M}_{55} \end{array} \right\} \left\{ \begin{array}{c} \mathcal{E}_x \\ \mathcal{E}_y \\ \gamma_{xy} \\ \gamma_{yz} \\ \gamma_{xz} \end{array} \right\}, \tag{26}$$

where

$$\mathfrak{M}_{11} = \frac{E_{nAl_2O_3}}{1-\left(\upsilon_{nAl_2O_3}\right)^2},\ \mathfrak{M}_{12} = \frac{\upsilon_{nAl_2O_3} E_{nAl_2O_3}}{1-\left(\upsilon_{nAl_2O_3}\right)^2},\ \mathfrak{M}_{22} = \frac{E_{nAl_2O_3}}{1-\left(\upsilon_{nAl_2O_3}\right)^2}, \tag{27}$$

$$\mathfrak{M}_{44} = \mathfrak{M}_{55} = \mathfrak{M}_{66} = \frac{E_{nAl_2O_3}}{2\left(1+\upsilon_{nAl_2O_3}\right)}. \tag{28}$$

Equations of motion

Hamilton's principle serves as the basis for deriving the motion equations corresponding to the newly proposed sinusoidal deformation shear theory. The expression for virtual strain energy is given by:

$$\delta \prod\nolimits_e = \int_A \int_{-\frac{h}{2}}^{\frac{h}{2}} (s_x \delta \mathrm{E}_x + s_y \delta \mathrm{E}_y + s_{xy} \delta \gamma_{xy} + s_{xz} \delta \gamma_{\{xz} + s_{yz} \delta \gamma_{yz}) d\mathcal{Z} dA. \tag{29}$$

Substituting Eq. (27) into Eq. (29) yields:

$$\delta \prod\nolimits_e = \int_A \int_{-\frac{h}{2}}^{\frac{h}{2}} \left\{ \begin{array}{c} \sigma_x(\delta \mathrm{E}_x^0 + Z\delta k_x^1 + f(z)\delta k_x^3) + \sigma_y(\delta \mathrm{E}_y^0 + Z\delta k_y^1 + f(z)\delta k_y^3) \\ +\sigma_{xy}(\delta \gamma_{xy}^0 + Z\delta k_{xy}^1 + f(z)\delta k_{xy}^3) + \sigma_{xz}(g(Z)\delta k_{xz}^2) \\ +\sigma_{yz}(g(Z)\delta k_{yz}^2) \end{array} \right\} = \int_A \left\{ \begin{array}{c} (_x\delta \mathrm{E}_x^0 + _x\delta k_x^1 + _x\delta k_x^3) + (_y\delta \mathrm{E}_y^0 + _y\delta k_y^1 + _y\delta k_y^3) \\ +(_{xy}\delta \gamma_{xy}^0 + _{xy}\delta k_{xy}^1 + _{xy}\delta k_{xy}^3) \\ +(_{xz}\delta k_{xz}^2) + (_{yz}\delta k_{yz}^2) \end{array} \right\} dA \tag{30}$$

where

$$(\mathbb{n}_i, \mathbb{m}_i, \mathbb{p}_i) = \int_{-\frac{h}{2}}^{\frac{h}{2}} \sigma_i(1, \mathcal{Z}, f(z))\, d\mathcal{Z} \qquad \{i = \mathcal{X}, y, \mathcal{X}y\} \tag{31}$$

$$(\mathbb{q}_i) = \int_{-\frac{h}{2}}^{\frac{h}{2}} \sigma_i((\mathcal{Z}))\, d\mathcal{Z}, \qquad j = \mathcal{X}\mathcal{Z}, y\mathcal{Z} \tag{32}$$

Substituting Eqs. (13a), (13b), (13c), and (14) in Eqs. (18a), and (18b) leads to:

$$\left\{ \begin{array}{c} n \\ m \\ p \end{array} \right\} = \left[\begin{array}{ccc} [\mathfrak{A}] & [\mathfrak{B}] & [\mathfrak{D}] \\ [\mathfrak{B}] & [\mathfrak{C}] & [\mathfrak{E}] \\ [\mathfrak{D}] & [\mathfrak{E}] & [\mathfrak{G}] \end{array} \right] \left\{ \begin{array}{c} \mathcal{E}^0 \\ k^1 \\ k^3 \end{array} \right\}, \tag{33}$$

$$\{\mathbb{q}\} = [\mathfrak{A}_s]\{\gamma^0\}, \tag{34}$$

where

$$[\mathfrak{A}] = \left[\begin{array}{ccc} \mathfrak{A}_{11} & \mathfrak{A}_{12} & 0 \\ \mathfrak{A}_{12} & \mathfrak{A}_{22} & 0 \\ 0 & 0 & \mathfrak{A}_{66} \end{array} \right],\ [\mathfrak{B}] = \left[\begin{array}{ccc} \mathfrak{B}_{11} & \mathfrak{B}_{12} & 0 \\ \mathfrak{B}_{12} & \mathfrak{B}_{22} & 0 \\ 0 & 0 & \mathfrak{B}_{66} \end{array} \right],\ [\mathfrak{C}] = \left[\begin{array}{ccc} \mathfrak{C}_{11} & \mathfrak{C}_{12} & 0 \\ \mathfrak{C}_{12} & \mathfrak{C}_{22} & 0 \\ 0 & 0 & \mathfrak{C}_{66} \end{array} \right], \tag{35}$$

$$[\mathfrak{D}] = \left[\begin{array}{ccc} \mathfrak{D}_{11} & \mathfrak{D}_{12} & 0 \\ \mathfrak{D}_{12} & \mathfrak{D}_{22} & 0 \\ 0 & 0 & \mathfrak{D}_{66} \end{array} \right],\ [\mathfrak{E}] = \left[\begin{array}{ccc} \mathfrak{E}_{11} & \mathfrak{E}_{12} & 0 \\ \mathfrak{E}_{12} & \mathfrak{E}_{22} & 0 \\ 0 & 0 & \mathfrak{E}_{66} \end{array} \right],\ [\mathfrak{G}] = \left[\begin{array}{ccc} \mathfrak{G}_{11} & \mathfrak{G}_{12} & 0 \\ \mathfrak{G}_{12} & \mathfrak{G}_{22} & 0 \\ 0 & 0 & \mathfrak{G}_{66} \end{array} \right], \tag{36}$$

$$[\mathfrak{A}_s] = \left[\begin{array}{cc} \mathfrak{A}_{44} & 0 \\ 0 & \mathfrak{A}_{55} \end{array} \right],\ [\mathfrak{C}_s] = \left[\begin{array}{cc} \mathfrak{C}_{44} & 0 \\ 0 & \mathfrak{C}_{55} \end{array} \right],\ [\mathfrak{E}_s] = \left[\begin{array}{cc} \mathfrak{E}_{44} & 0 \\ 0 & \mathfrak{E}_{55} \end{array} \right], \tag{37}$$

$$(\mathfrak{A}_{ij}, \mathfrak{B}_{ij}, \mathfrak{C}_{ij}, \mathfrak{D}_{ij}, \mathfrak{E}_{ij}, \mathfrak{G}_{ij}) = \int_{-\frac{h}{2}}^{\frac{h}{2}} \mathfrak{q}_{ij}(1, \mathcal{Z}, \mathcal{Z}^2, f(\mathcal{Z}), \mathcal{Z}f(\mathcal{Z}), f^2(\mathcal{Z}))\, \mathrm{d}\mathcal{Z}, (i, j = 1\text{to}6), \tag{38}$$

$$(\mathfrak{A}_{sij}) = \int_{-\frac{h}{2}}^{\frac{h}{2}} \mathfrak{q}_{ij}\,(\mathfrak{g}(\mathcal{Z}))\, \mathrm{d}\mathcal{Z}, (ij = 44{,}55). \tag{39}$$

To establish a direct coupling between the supersonic aerodynamic pressure and the elastic foundation parameters, the classical first-order piston theory is modified. The localized aero-elastic interaction factor ($\wedge_f$) is introduced to couple the normal foundation stiffness directly into the aerodynamic pressure wave propagation equation as follows:

$$\wedge_f = 1 + \alpha_c \left(\frac{K_{wo} a^4}{D_0} - \frac{K_{po} a^2}{D_0} \nabla^2 \right). \tag{40}$$

where α_c is the non-dimensional aerodynamic-foundation coupling scaling parameter, a is the panel length, and D_0 represents the reference bending rigidity of the hybrid nano-composite structure. Consequently, the directly coupled supersonic aerodynamic piston pressure $\Delta p_{Coupled}$ acting on the doubly-curved fuselage panel is derived as:

$$\Delta p_{Coupled} = -2q_\infty \beta \wedge_f \left(\frac{\partial w}{\partial x} + \frac{M_\infty^2 - 2}{M_\infty^2 - 1} \frac{1}{U_\infty} \frac{\partial w}{\partial t} \right), \tag{41}$$

where

$$q_\infty = \frac{1}{2} \rho_\infty U_\infty^2, \tag{42}$$

$$\beta = \sqrt{(M_\infty^2 - 1)}. \tag{43}$$

In these expressions, ρ_∞ and U_∞ represent the airflow density and velocity, respectively. In the context of first-order piston theory, the Mach number U_∞ typically falls within the range of $\sqrt{2}$ to 5.0. For supersonic flow conditions where M_∞ is significantly greater than 1, the term $[(M_\infty^2 - 2)/(M_\infty^2 - 1)]\,\kappa/\sqrt{M_\infty^2 - 1} \to \kappa/M_\infty$ simplifies to κ/M_∞, with κ defined as $\rho_\infty a/\rho_m h$. The aerodynamic damping parameter is subsequently taken as $\kappa/M_\infty = 0.01$ for the aeroelastic analysis that follows[39]. Additionally, the non-dimensional aerodynamic pressure employed in the same analysis is $\lambda = 2q_\infty a^3/\beta D$, where $D = E_m h^3/[12(1 - \theta_m^2)]$. It can be observed from Eq. (21) that when the foundation parameters drop to zero (K_{wo}, K_{po}), the interaction factor becomes unity ($\wedge_f = 1$), and the formulation rigorously simplifies back to the classical uncoupled supersonic piston theory. The total virtual work performed by the combined coupled aerodynamic forces and the parameter-dependent in-plane elastic foundation interactions (Π_v) is evaluated via:

$$\Pi_v = \int \left(\Delta p_{Coupled} w + F_f w_0 + F_r v_0 \right) dA. \tag{44}$$

The virtual kinetic energy is given by:

$$\delta \prod_k = \int_A \int_{-\frac{h}{2}}^{\frac{h}{2}} \rho n Al_2O_3(z)(\dot{u}\delta\dot{u} + \dot{v}\delta\dot{v} + \dot{w}\delta\dot{w})\, dZ\mathrm{d}\mathfrak{A} = \int_A \left\{ \begin{array}{l} \mathcal{L}_0(\dot{u}_0\delta\dot{u}_0 + \dot{v}_0\delta\dot{w}_0 + \dot{w}_0\delta\dot{w}_0) \\ -\mathcal{L}_1\left(\dot{u}_0\frac{\partial\delta\dot{w}_0}{\partial x} + \frac{\partial\dot{w}_0}{\partial x}\delta\dot{u}_0 + \dot{v}_0\frac{\partial\delta\dot{w}_0}{\partial y} + \frac{\partial\dot{w}_0}{\partial y}\delta\dot{v}_0\right) \\ +\mathcal{L}_2\left(\frac{\partial\dot{w}_0}{\partial x}\frac{\partial\delta\dot{w}_0}{\partial x} + \frac{\partial\dot{w}_0}{\partial y}\frac{\partial\delta\dot{w}_0}{\partial y}\right) \\ +\mathcal{L}_3\left(\dot{u}_0\delta\dot{\theta}_x + \delta\dot{u}_0\dot{\theta}_x + \dot{v}_0\delta\dot{\theta}_y + \delta\dot{v}_0\dot{\theta}_y\right) \\ -\mathcal{L}_4\left(\frac{\partial\dot{w}_0}{\partial x}\delta\dot{\theta}_x + \frac{\partial\delta\dot{w}_0}{\partial x}\dot{\theta}_x + \frac{\partial\dot{w}_0}{\partial y}\delta\dot{\theta}_y\right) \\ +\mathcal{L}_5\left(\dot{\theta}_x\delta\dot{\theta}_x + \dot{\theta}_y\delta\dot{\theta}_y\right) \end{array} \right\} dA, \tag{45}$$

where mass inertias are defined by:

$$\{\mathcal{L}_0, \mathcal{L}_1, \mathcal{L}_2, \mathcal{L}_3, \mathcal{L}_4, \mathcal{L}_5\} = \int_{-\frac{h}{2}}^{\frac{h}{2}} \rho_{nAl_2O_3}(Z)\left\{1, Z, Z^2, f(z), Zf(z), (f(z))^2\right\} \mathrm{d}Z. \tag{46}$$

The contribution of the Winkler-Pasternak foundation to the total energy is expressed as follows:[57]:

$$\delta\Pi_w = \frac{1}{2}\int \left(-K_{wo}w_0 + \left(\frac{\partial}{\partial x}\left(\frac{\partial w_0}{\partial x}K_{po}\right) + \frac{\partial}{\partial y}\left(\frac{\partial w_0}{\partial y}K_{po}\right)\right)\right) w_0 dA, \tag{47}$$

In these expressions, K_{wo} represents the Winkler modulus, while K_{po} stands for the Pasternak modulus of the elastic foundation. The energy resulting from the torsional elastic foundation is given in the following manner[58]:

$$\delta\Pi_T = \frac{1}{2}\int \left(K_{r10}\phi - \frac{\partial}{\partial x}\left(K_{r20}\frac{\partial\phi}{\partial x}\right)\right) w_0 dA, \tag{48}$$

The quantities K_{r10}, and K_{r20} are the torsional coefficients associated with the foundation. By replacing ϕ with $(\frac{\partial w_0}{\partial x})$ in Eq. (28), we obtain:

$$\delta\Pi_r = \frac{1}{2}\int \left(K_{r10}\frac{\partial w_0}{\partial x} - \frac{\partial}{\partial x}\left(K_{r20}\frac{\partial^2 w_0}{\partial x^2}\right)\right) w_0 dA, \tag{49}$$

$$F_r = K_{r10}\frac{\partial w_0}{\partial x} - \frac{\partial}{\partial x}\left(K_{r20}\frac{\partial^2 w_0}{\partial x^2}\right).$$

The contribution of the frictional force to the total work can be written as[58]:

$$\delta\Pi_f = \frac{1}{2}\int \mu_f\left(-K_{wo}w_0 + \left(\frac{\partial}{\partial x}\left(\frac{\partial w_0}{\partial x}K_{po}\right) + \frac{\partial}{\partial y}\left(\frac{\partial w_0}{\partial y}K_{po}\right)\right)\right) w_0 dA, \tag{50}$$

$$F_f = \mu_f\left(-K_{wo}w_0 + \left(\frac{\partial}{\partial x}\left(\frac{\partial w_0}{\partial x}K_{po}\right) + \frac{\partial}{\partial y}\left(\frac{\partial w_0}{\partial y}K_{po}\right)\right)\right).$$

In this equation, μ_f represents the coefficient of friction for the foundation. The amount of energy dissipated through the damper foundation is given by the following expression[57]:

$$\Pi_D = \frac{1}{2}\int C_{do}\left(\frac{\partial w_0}{\partial t}\right)^2 dA. \tag{51}$$

In this context, C_{do} represents the damping coefficient associated with the viscoelastic material. The present study adopts a linear damping model for the viscoelastic foundation, owing to its simple mathematical structure

and computational convenience, rendering it suitable for cases involving small to moderate deformations. The parameters appearing in Eqs. (27), (29), (30), and (31) are given by:

$$\begin{aligned}
K_{wo} &= K_w\left(1+f_1\left(\frac{x}{a}\right)+f_2\left(\frac{x}{a}\right)^2+f_3\left(\frac{x}{a}\right)^3+f_4\left(\frac{x}{a}\right)^4\right),\\
K_{po} &= K_p\left(1+f_1\left(\frac{x}{a}\right)+f_2\left(\frac{x}{a}\right)^2+f_3\left(\frac{x}{a}\right)^3+f_4\left(\frac{x}{a}\right)^4\right),\\
C_{do} &= C_d\left(1+f_1\left(\frac{x}{a}\right)+f_2\left(\frac{x}{a}\right)^2+f_3\left(\frac{x}{a}\right)^3+f_4\left(\frac{x}{a}\right)^4\right),\\
K_{r10} &= K_{r1}\left(1+f_1\left(\frac{x}{a}\right)+f_2\left(\frac{x}{a}\right)^2+f_3\left(\frac{x}{a}\right)^3+f_4\left(\frac{x}{a}\right)^4\right),\\
K_{r20} &= K_{r2}\left(1+f_1\left(\frac{x}{a}\right)+f_2\left(\frac{x}{a}\right)^2+f_3\left(\frac{\ominus x}{a}\right)^3+f_4\left(\frac{x}{a}\right)^4\right).
\end{aligned} \tag{52}$$

The constants f_1, f_2, f_3 and f_4 describe variations in stiffness along the x direction — specifically, linear, quadratic, and cubic forms (with f3 and f4 also capturing linear and quadratic components, respectively, as implied by the original phrasing). K_w is the elastic coefficient of the Winkler foundation situated at the bottom center of the panel. K_p denotes the elastic coefficient of the Pasternak foundation at the same bottom-center location. K_{r1} and K_{r2} are the elastic coefficients of the torsional foundation at the panel's bottom center. C_d represents the elastic coefficient of the damping foundation at the bottom center. The analytical form of Hamilton's principle is then written as:

$$\int_0^T \left(\delta \Pi_k - \left(\delta \Pi_e - \delta \Pi_v - \delta \Pi_w - \delta \Pi_r - \delta \Pi_f + \dot{\delta} \Pi_D\right)\right)\mathrm{d}t = 0, \tag{53}$$

Substituting Eqs. (17), (24), (25), (27), (29), (30), and (31) into Eq. (33), followed by integration by parts, yields the following Euler–Lagrange equations:

$$\delta u_0 : \frac{\partial N_{xx}}{\partial x}+\frac{\partial N_{xy}}{\partial y}+F_f = \mathcal{L}_0 \ddot{w}_0 - \mathcal{L}_1 \frac{\partial \ddot{w}_0}{\partial x}+\mathcal{L}_3 \ddot{\theta}_x, \tag{54}$$

$$\delta v_0 : \frac{\partial N_{xy}}{\partial x}+\frac{\partial N_{yy}}{\partial y}-K_{r10}\frac{\partial v_0}{\partial \mathcal{X}}+\frac{\partial}{\partial \mathcal{X}}\left(K_{r20}\frac{\partial^2 v_0}{\partial \mathcal{X}^2}\right) = \mathcal{L}_0 \ddot{v}_0 - \mathcal{L}_1 \frac{\partial \ddot{w}_0}{\partial y}+\mathcal{L}_3 \ddot{\theta}_y, \tag{55}$$

$$\begin{aligned}
&\delta w_0 : \frac{\partial^2 M_{xx}}{\partial x^2}+2\frac{\partial^2 M_{xy}}{\partial x \partial y}+\frac{\partial^2 M_{yy}}{\partial y^2}+\left(\frac{N_{xx}}{R_{\mathcal{X}}}+\frac{N_{yy}}{R_y}\right)+\frac{\partial}{\partial \mathcal{X}}\left(N_{xx}\frac{\partial w_0}{\partial \mathcal{X}}+N_{xy}\frac{\partial w_0}{\partial y}\right)\\
&+\frac{\partial}{\partial y}\left(N_{yy}\frac{\partial w_0}{\partial y}+N_{xy}\frac{\partial w_0}{\partial \mathcal{X}}\right)+\Delta p_{Coupled}-K_{wo}w_0+\left(\frac{\partial}{\partial \mathcal{X}}\left(\frac{\partial w_0}{\partial \mathcal{X}}K_{po}\right)+\frac{\partial}{\partial y}\left(\frac{\partial w_0}{\partial y}K_{po}\right)\right)\\
&-C_{do}\dot{w}_0 = \mathcal{L}_1\left(\frac{\partial \ddot{w}_0}{\partial x}+\frac{\partial \ddot{w}_0}{\partial y}\right)-\mathcal{L}_2\left(\frac{\partial^2 \ddot{w}_0}{\partial x^2}+\frac{\partial^2 \ddot{w}_0}{\partial y^2}\right)+\mathcal{L}_4\left(\frac{\partial \ddot{\theta}_x}{\partial x}+\frac{\partial \ddot{\theta}_y}{\partial y}\right)+\mathcal{L}_0 \ddot{w}_0,
\end{aligned} \tag{56}$$

$$\delta \theta_x : \frac{\partial P_{xx}}{\partial x}+\frac{\partial P_{xy}}{\partial y}-Q_{xx} = \mathcal{L}_3 \ddot{u}_0 - \mathcal{L}_4 \frac{\partial \ddot{u}_0}{\partial x}+\mathcal{L}_5 \ddot{\theta}_x, \tag{57}$$

$$\delta \theta_y : \frac{\partial P_{yy}}{\partial y}+\frac{\partial P_{xy}}{\partial y}-Q_{yy} = \mathcal{L}_3 \ddot{v}_0 - \mathcal{L}_4 \frac{\partial \ddot{w}_0}{\partial y}+\mathcal{L}_5 \ddot{\theta}_y. \tag{58}$$

Limitations and assumptions of the study

These are some of the main assumptions made in the current analysis methodology. First of all, it is assumed that the nano alumina/epoxy composite is macroscopically homogeneous in nature, with a perfect interfacial bond between nanoparticles and matrix, neglecting agglomeration and/or formation of any voids. The higher-order shear deformation theory with hyperbolic shape function assumes that transverse shear strains have a specific distribution, which does not cover all the higher-order effects in very thick panels. In addition, von Kármán geometric nonlinearities are applied for moderate rotations, hence excluding large deformations or post-buckling conditions. It should be mentioned that first-order piston theory applies only to supersonic flow with Mach number between $\sqrt{2}$ and 5, and small disturbances, hence cannot be used for hypersonic or highly separated flows. The viscoelastic foundation is considered as linear damping only, and stiffness variations are considered in polynomial form (up to quartic). The harmonic balance approach includes only cosine terms up to the sixth order. Finally, the current research is only analytical, and experimental verification is lacking. Seventh, the damping of the viscoelastic foundation is considered with the help of a linear viscous damper, meaning that the dissipation force is proportional to the velocity and not dependent on the frequency and amplitude of oscillation. Such an approach is justified for small to moderate displacements and certain frequency ranges. However, at large deformation or over a broad frequency range, the effects of nonlinear damping should be considered (for example, hysteretic or fractional order damping). Thus, the present linear approach provides a simplified model, and its extrapolation to highly nonlinear regimes should be treated cautiously. Furthermore, while the first-order piston theory is applied to describe the aerodynamic loadings and modal coalescence is analyzed as a precursor of fluttering, in the present research, no complete aeroelastic eigenvalue problem is solved, and no exact flutter boundaries are calculated. The concepts of 'flutter resistance' and 'aeroelastic stability' are used here in a limited sense to denote the retardation of the coalescence of the first two modal frequencies (Figs. 7, 8, 9, 10, 11, 12, 13, 14, 15 and 16).

Input parameters and geometric assumptions

All simulation results presented in Sect. 5 are obtained using the baseline parameters listed in Table 2. The double curvature is shallow, meaning R_x, $R_y \gg a, b$, and the thickness-to-length ratio satisfies $h/a \leq 0.13$. The

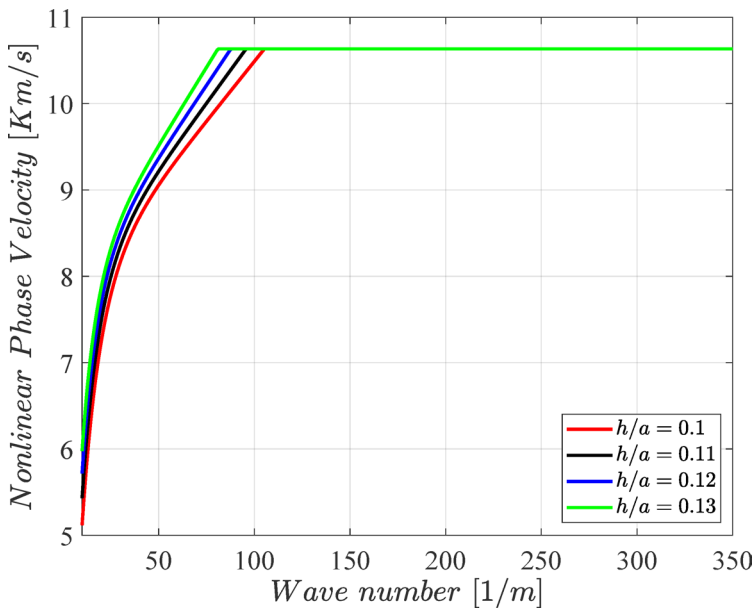


Fig. 7 The effect of the panel's thickness-to-length ratio on NPV as a function of wave number.

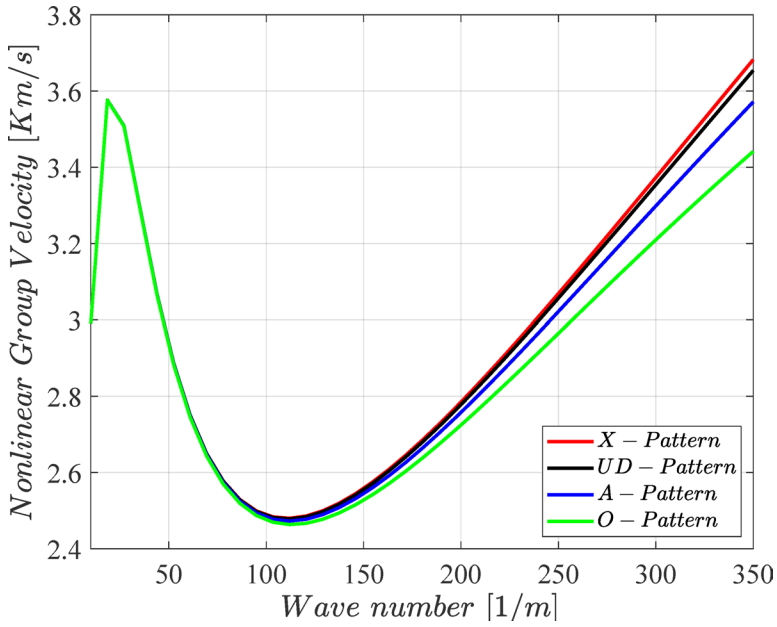


Fig. 8 The influence of different nano-alumina distribution patterns on the NGV as a function of wave number.

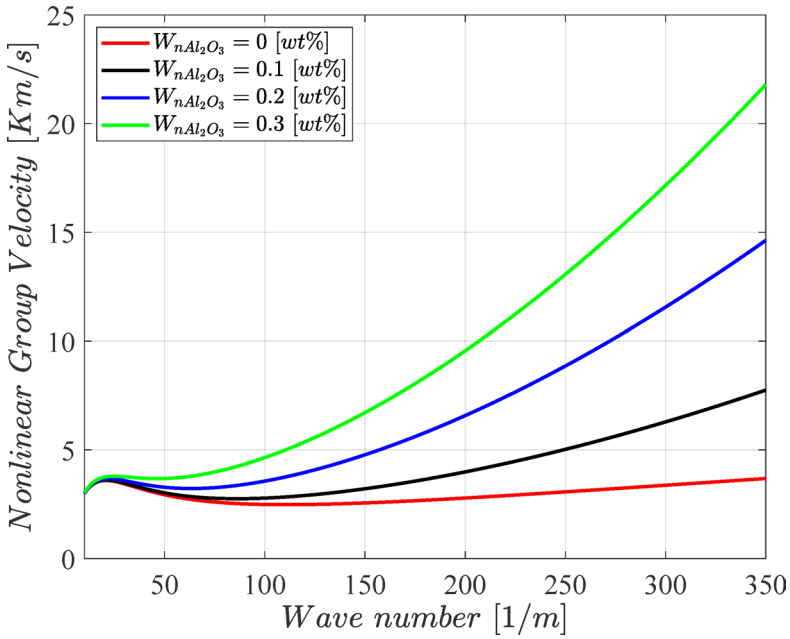


Fig. 9 The influence of different nano-alumina weight fractions on the NGV as a function of wave number.

aerodynamic flow is supersonic, with the Mach number taken as $M_\infty = 2.5$ (unless otherwise stated), and the non-dimensional aerodynamic pressure λ is varied as indicated in each figure.

Solution procedure

Taking into account the geometric and boundary conditions of the problem, the displacement may be conveniently written in terms of a harmonic function as follows:

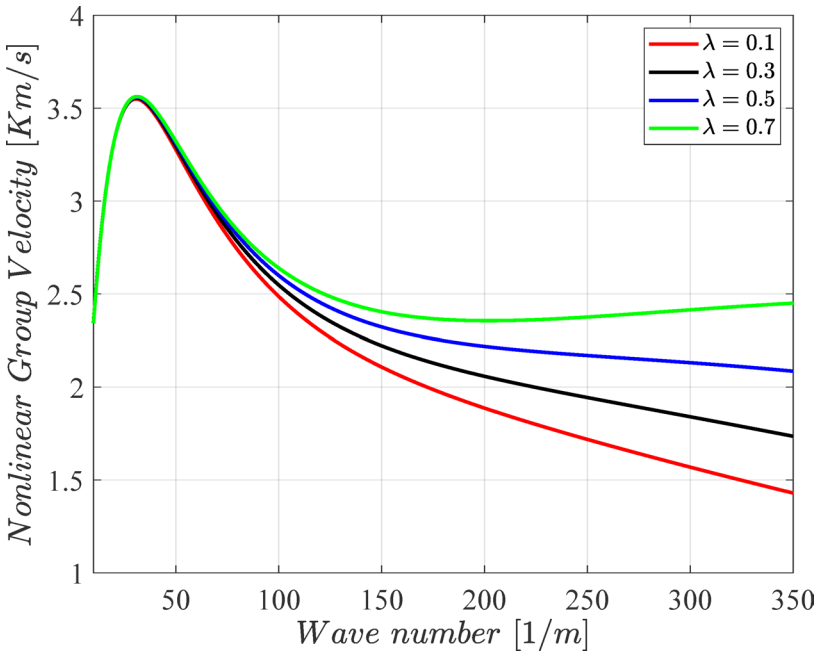


Fig. 10 The influence of different aerodynamic pressures on the NGV as a function of wave number.

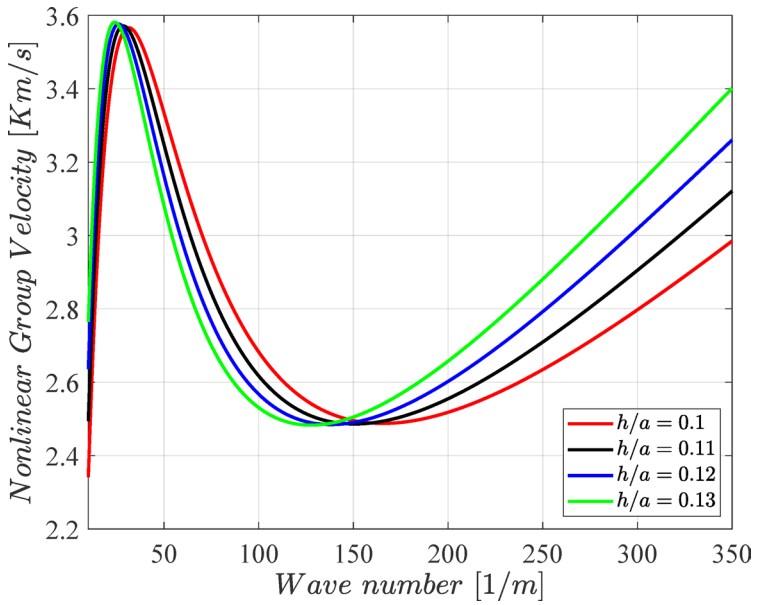


Fig. 11 The influence of the panel's thickness-to-length ratio on the nonlinear group velocity as a function of wave number.

https://doi.org/10.1038/s41598-026-71917-0

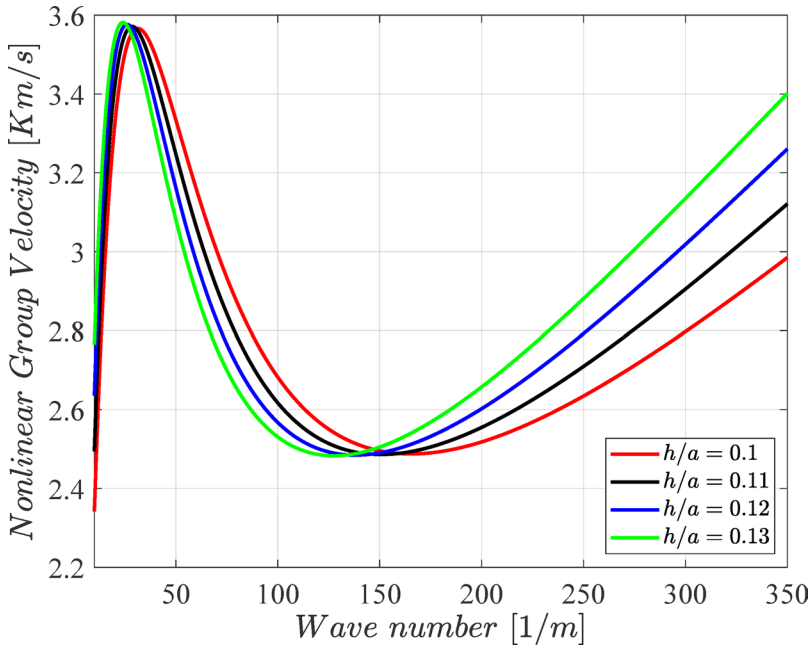


Fig. 12 The influence of different nano-alumina distribution patterns on the nonlinear velocity ratio as a function of wave number.

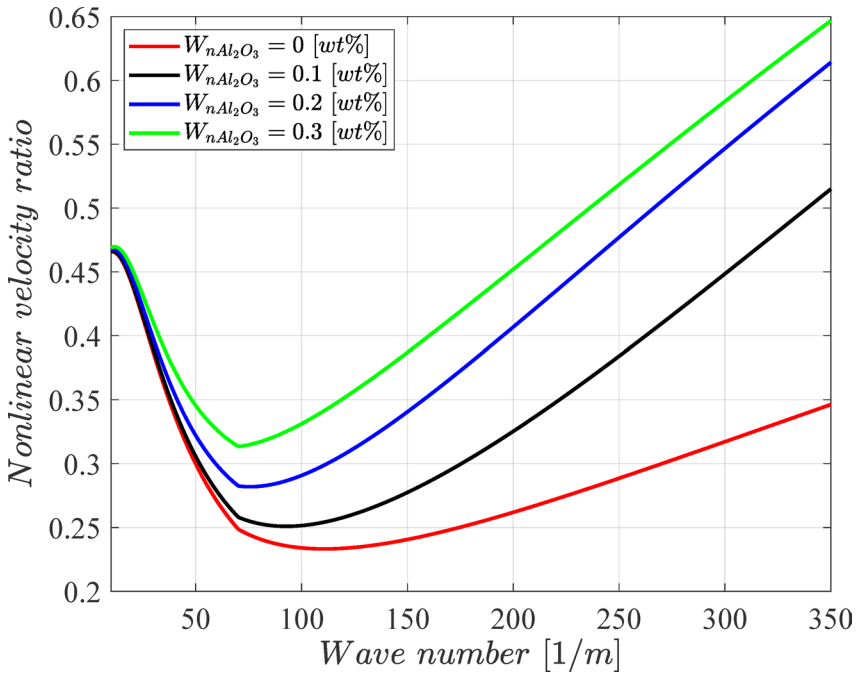


Fig. 13 The influence of different nano-alumina weight fractions on the nonlinear velocity ratio as a function of wave number.

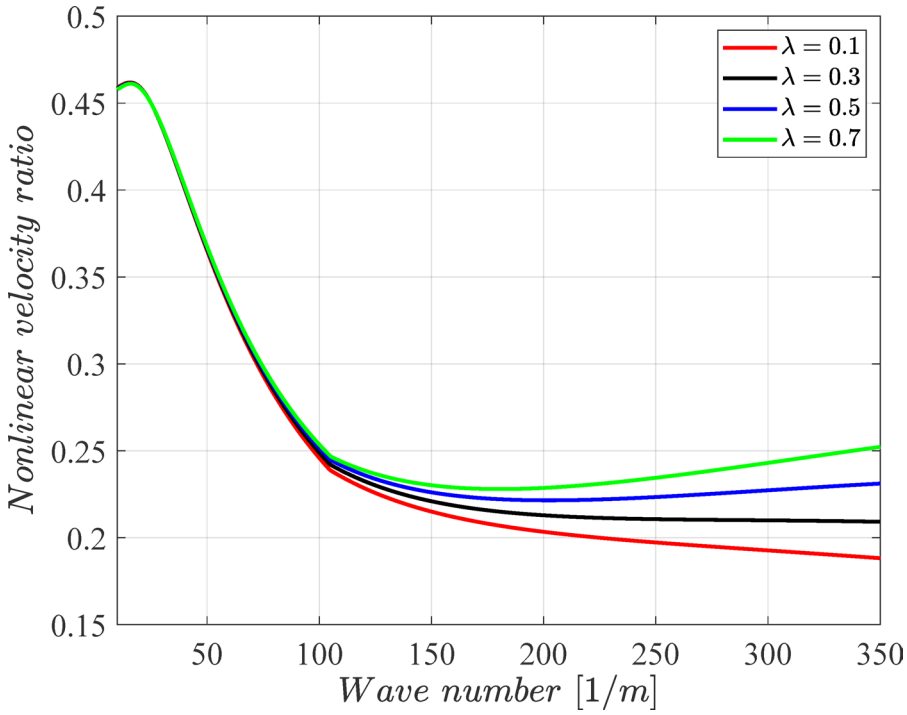


Fig. 14 The influence of different aerodynamic pressures on the nonlinear velocity ratio as a function of wave number.

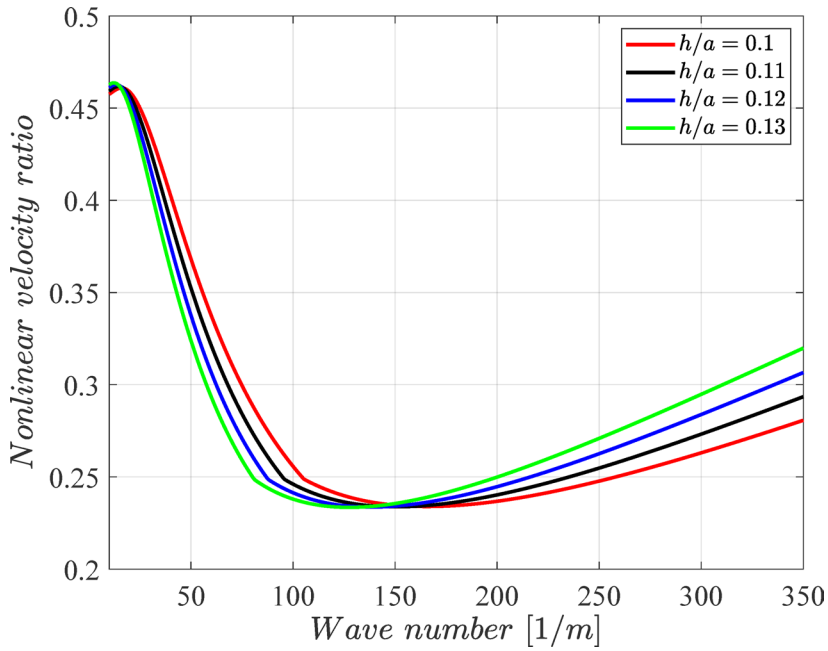


Fig. 15 The effect of the panel's thickness-to-length ratio on the nonlinear velocity ratio across a range of wave numbers.

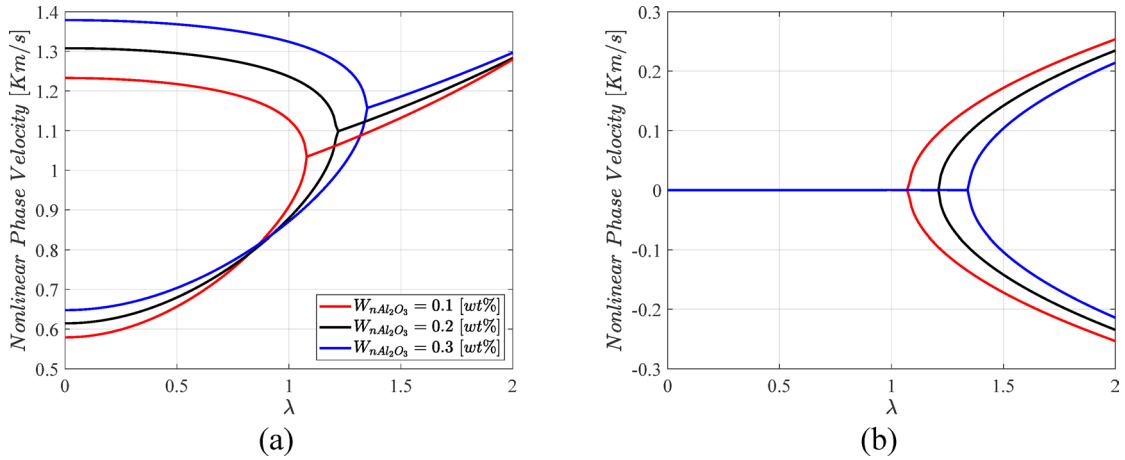


Fig. 16 The NPV response to varying aerodynamic pressure (λ) conditions and nanocomposite weight fraction.

Table 2 All simulation results presented in Sect. 5 are obtained using the baseline parameters listed in this table.

Parameter	Symbol	Value (baseline)
Panel length (x-direction)	a	0.5 m
Panel width (y-direction)	b	0.4 m
Panel thickness	h	0.05 m
Radii of curvature	R_x, R_y	2.0 m, 2.5 m
Winkler stiffness (baseline)	K_w	2.5×10^6 N/m^3
Pasternak stiffness (baseline)	K_p	1.2×10^5 N/m
Torsional coefficients (baseline)	K_{r1}, K_{r2}	50 N/m, 10 N
Damping coefficient (baseline)	C_d	3 $N\cdot s/m^2$
Friction coefficient	μ_f	0.2 (dimensionless)
Aerodynamic Mach number	M_∞	2.5
Air density	ρ_∞	1.225 kg/m^3
Non-dimensional aerodynamic pressure range	λ	0.1–0.7 (Figs. 7, 11 and 15), 0–2.0 (Figs. 17, 18, 19 and 20)
Nano- $Al?O?$ weight fraction range	$W_{nAl_2O_3}$	0–0.3 (0 $wt\%$, 0.1, 0.2, 0.3)
Wave number range	k	40–350 m^{-1}

$$\begin{aligned} u_0 &= U_0\exp(kx+ky)\,i, \quad & v_0 &= V_0\exp(kx+ky)\,i,\\ w_0 &= W_0\exp(kx+ky)\,i, \quad & \theta_x &= \bar{\theta}_x\exp(kx+ky)\,i,\\ \theta_y &= \bar{\theta}_y\exp(kx+ky)\,i, \end{aligned} \tag{59}$$

Replacing Eq. (35) within Eqs. (34a–e) allows one to derive a system of ordinary differential Equations.

$$\begin{aligned} &\mathbb{K}_{11}u_0(t)+\mathbb{K}_{12}v_0(t)+\mathbb{K}_{13}w_0(t)+\mathbb{K}_{14}w_0^2(t)\\ &+\mathbb{K}_{15}\theta_x^-(t)+\mathbb{K}_{16}\theta_x^-(t)=\mathbb{M}_{11}\ddot{u}_0(t)\\ &+\{\mathbb{M}\}\,12\ddot{v}_0(t)+\mathbb{M}_{13}\ddot{w}_0(t)\\ &+\mathbb{M}_{14}\ddot{\underset{x}{\theta}}(t)+\mathbb{M}_{15}\ddot{\underset{x}{\theta}}(t) \end{aligned} \tag{60}$$

$$\begin{aligned} &\mathbb{K}_{21}u_0(t)+\mathbb{K}_{22}v_0(t)+\mathbb{K}_{23}w_0(t)+\mathbb{K}_{24}w_0^2(t)+\mathbb{K}_{25}\bar{\theta}_x(t)+\mathbb{K}_{26}\bar{\theta}_y(t)=\\ &\mathbb{M}_{21}\ddot{u}_0(t)+\mathbb{M}_{22}\ddot{v}_0(t)+\mathbb{M}_{23}\ddot{w}_0(t)+\mathbb{M}_{24}\ddot{\bar{\theta}}_x(t)+\mathbb{M}_{25}\ddot{\bar{\theta}}_y(t) \end{aligned} \tag{61}$$

$$\mathbb{K}_{31}u_0(t)+\mathbb{K}_{32}v_0(t)+\mathbb{K}_{33}w_0(t)+\mathbb{K}_{34}\dot{w}_0(t)+\mathbb{K}_{35}w_0^2(t)+\mathbb{K}_{36}w_0^3(t)+\mathbb{K}_{37}\bar{\theta}_x(t)+\mathbb{K}_{38}\bar{\theta}_y(t)=\mathbb{M}_{31}\ddot{u}_0(t)+\mathbb{M}_{32}\ddot{v}_0(t)+\mathbb{M}_{33}\ddot{w}_0(t)+\mathbb{M}_{34}\ddot{\bar{\theta}}_y(t)+\mathbb{M}_{35}\ddot{\bar{\theta}}_y(t) \tag{62}$$

$$\begin{aligned}&\mathbb{K}_{31}u_0(t)+\mathbb{K}_{32}v_0(t)+\mathbb{K}_{33}w_0(t)+\mathbb{K}_{34}\dot{w}_0(t)\\&+\mathbb{K}_{35}w_0^2(t)+\mathbb{K}_{36}w_0^3(t)+\mathbb{K}_{37}\bar{\theta}_x(t)+\mathbb{K}_{38}\bar{\theta}_y(t)\\&=\mathbb{M}_{31}\ddot{u}_0(t)+\mathbb{M}_{32}\ddot{v}_0(t)+\mathbb{M}_{33}\ddot{w}_0(t)\\&+\mathbb{M}_{34}\ddot{\bar{\theta}}_x(t)+\mathbb{M}_{35}\ddot{\bar{\theta}}_y(t)\end{aligned} \tag{63}$$

$$\begin{aligned}&\mathbb{K}_{51}u_0(t)+\mathbb{K}_{52}v_0(t)+\mathbb{K}_{53}w_0(t)\\&+\mathbb{K}_{54}w_0^2(t)+\mathbb{K}_{55}\bar{\theta}_x(t)+\mathbb{K}_{56}\bar{\theta}_y(t)\\&=\mathbb{M}_{51}\ddot{u}_0(t)+\mathbb{M}_{52}\ddot{v}_0(t)+\mathbb{M}_{53}\ddot{w}_0(t)\\&+\mathbb{M}_{54}\ddot{\bar{\theta}}_x(t)+\mathbb{M}_{55}\ddot{\bar{\theta}}_y(t)\end{aligned} \tag{64}$$

Because the effects of the damping and inertial contributions — namely $\dot{w}_0(t)$, $\ddot{u}_0(t)$, $\ddot{v}_0(t)$, $\ddot{w}_0(t)$, $\ddot{\bar{\theta}}_x(t)$, and $\ddot{\bar{\theta}}_y(t)$ — are negligibly small, they are excluded from Eqs. (36a), (36b), (36d), and (36e). After solving these modified equations, the obtained solutions are then inserted back into Eq. (36c).

$$\ddot{w}_0(t)+\tilde{\mathbb{J}}_1\dot{w}_0(t)+\tilde{\mathbb{J}}_2w_0(t)+\tilde{\mathbb{J}}_3w_0^2(t)+\tilde{\mathbb{J}}_4w_0^3(t)=0, \tag{65}$$

In this context, the quantities $\tilde{\mathbb{J}}_1$ to $\tilde{\mathbb{J}}_4$ encompass the linear as well as the nonlinear parts of w_0. According to the harmonic balance approach[43,44], an approximation for w₀ is given by the following expression:

$$w_0(t)=e^{\mathbb{C}t}\sum_{k=0}^{M}\mathbb{A}_k cos(\mathbb{B}\eta) \tag{66}$$

Within this framework, $\mathbb{A}_1$ is a constant, whereas the quantities $\mathbb{A}_i$ (with $i=0,2,3,\ldots,M$) are unknown functions that vary with time. The constant $\mathbb{C}$ equals $-\frac{1}{2}\tilde{\mathbb{J}}_1$, and η is defined as $\omega t+\theta$, where θ is the initial phase angle, and ω stands for the nonlinear natural frequency of the panels. Because the oscillation amplitude depends on ω, this frequency changes over time under damped conditions, leading to $\omega=\omega(t)$. For the subsequent analysis, the value of M appearing in Eq. (38) is taken as six. Consequently, Eq. (38) takes the form presented below:

$$\tilde{W}(t)=e^{\mathbb{C}t}(\mathbb{A}_0+\mathbb{A}_1cos\eta+\mathbb{A}_2cos2\eta+\mathbb{A}_3cos3\eta+\mathbb{A}_4cos4\eta+\mathbb{A}_5cos5\eta+\mathbb{A}_6cos6\eta) \tag{67}$$

Inserting Eq. (39) into Eq. (37) and then setting the coefficients of $cos(\mathbb{B}\eta)$ to zero yields the equation shown below.

$$cos(\mathbb{B}\eta):\{\gamma_{11}-\mathbb{B}^2(\omega+t\frac{d\omega}{dt})^2\}\mathbb{A}_{\mathbb{B}}+\gamma_{12}e^{\mathbb{C}t}\mathbb{L}_{\mathbb{B}1}+\gamma_{13}e^{2\mathbb{C}t}\mathbb{L}_{\mathbb{B}2}=0,\ (\mathbb{B}=0,1,2,3,4,5,6) \tag{68}$$

where γ_{11} is defined as $\mathbb{C}^2+\tilde{\mathbb{J}}_1\mathbb{C}+\tilde{\mathbb{J}}_2$, γ_{12} equals $\tilde{\mathbb{J}}_3$, and γ_{13} equals $\tilde{\mathbb{J}}_5$; the symbols $\mathbb{L}_{\mathbb{B}1}$ and $\mathbb{L}_{\mathbb{B}2}$ denote the functions that depend on the parameter $\mathbb{A}_{\mathbb{B}}$, with their full forms given in Eqs. (41a) through (41u).

$$\mathbb{L}_{01}=\mathbb{A}_0^2+\frac{1}{2}\mathbb{A}_1^2+\frac{1}{2}\mathbb{A}_2^2+\frac{1}{2}\mathbb{A}_3^2+\frac{1}{2}\mathbb{A}_4^2+\frac{1}{2}\mathbb{A}_5^2+\frac{1}{2}\mathbb{A}_6^2 \tag{69}$$

$$\mathbb{L}_{11}=2\mathbb{A}_0\mathbb{A}_1+\mathbb{A}_1\mathbb{A}_2+\mathbb{A}_2\mathbb{A}_3+\mathbb{A}_3\mathbb{A}_4+\mathbb{A}_4\mathbb{A}_5+\mathbb{A}_5\mathbb{A}_6 \tag{70}$$

$$\mathbb{L}_{21}=\frac{1}{2}\mathbb{A}_1^2+\mathbb{A}_1\mathbb{A}_3+2\mathbb{A}_0\mathbb{A}_2+\mathbb{A}_2\mathbb{A}_4+\mathbb{A}_3\mathbb{A}_5+\mathbb{A}_4\mathbb{A}_6 \tag{71}$$

$$\mathbb{L}_{31} = 2\mathbb{A}_0\mathbb{A}_3 + \mathbb{A}_1\mathbb{A}_2 + \mathbb{A}_1\mathbb{A}_4 + \mathbb{A}_2\mathbb{A}_5 + \mathbb{A}_3\mathbb{A}_6 \tag{72}$$

$$\mathbb{L}_{41} = \frac{1}{2}\mathbb{A}_2^2 + \mathbb{A}_2\mathbb{A}_6 + 2\mathbb{A}_0\mathbb{A}_4 + \mathbb{A}_1\mathbb{A}_3 + \mathbb{A}_1\mathbb{A}_5 \tag{73}$$

$$\mathbb{L}_{51} = 2\mathbb{A}_0\mathbb{A}_5 + \mathbb{A}_1\mathbb{A}_4 + \mathbb{A}_2\mathbb{A}_3 + \mathbb{A}_1\mathbb{A}_6 \tag{74}$$

$$\mathbb{L}_{61} = \frac{1}{2}\mathbb{A}_3^2 + 2\mathbb{A}_0\mathbb{A}_6 + \mathbb{A}_1\mathbb{A}_5 + \mathbb{A}_2\mathbb{A}_4 \tag{75}$$

$$\begin{aligned}\mathbb{L}_{02} = {} & \mathbb{A}_0^3 + \frac{3}{4}\mathbb{A}_1^2\mathbb{A}_2 + \frac{3}{4}\mathbb{A}_2^2\mathbb{A}_4 + \frac{3}{4}\mathbb{A}_3^2\mathbb{A}_6 + \frac{3}{2}\mathbb{A}_0\mathbb{A}_1^2 + \frac{3}{2}\mathbb{A}_0\mathbb{A}_2^2 + \frac{3}{2}\mathbb{A}_0\mathbb{A}_3^2 + \frac{3}{2}\mathbb{A}_0\mathbb{A}_4^2 + \frac{3}{2}\mathbb{A}_0\mathbb{A}_5^2 \\ & + \frac{3}{2}\mathbb{A}_0\mathbb{A}_6^2 + \frac{3}{2}\mathbb{A}_1\mathbb{A}_2\mathbb{A}_3 + \frac{3}{2}\mathbb{A}_1\mathbb{A}_3\mathbb{A}_4 + \frac{3}{2}\mathbb{A}_1\mathbb{A}_4\mathbb{A}_5 + \frac{3}{2}\mathbb{A}_1\mathbb{A}_5\mathbb{A}_6 + \frac{3}{2}\mathbb{A}_2\mathbb{A}_3\mathbb{A}_5 + \frac{3}{2}\mathbb{A}_2\mathbb{A}_4\mathbb{A}_6\end{aligned} \tag{76}$$

$$\begin{aligned}\mathbb{L}_{12} = {} & \frac{3}{4}\mathbb{A}_1^3 + 3\mathbb{A}_0^2\mathbb{A}_1 + \frac{3}{4}\mathbb{A}_1^2\mathbb{A}_3 + \frac{3}{4}\mathbb{A}_2^2\mathbb{A}_3 + \frac{3}{4}\mathbb{A}_2^2\mathbb{A}_5 + \frac{3}{4}\mathbb{A}_3^2\mathbb{A}_5 + \frac{3}{2}\mathbb{A}_1\mathbb{A}_2^2 + \frac{3}{2}\mathbb{A}_1\mathbb{A}_3^2 \\ & + \frac{3}{2}\mathbb{A}_1\mathbb{A}_4^2 + \frac{3}{2}\mathbb{A}_1\mathbb{A}_5^2 + \frac{3}{2}\mathbb{A}_1\mathbb{A}_6^2 + 3\mathbb{A}_0\mathbb{A}_1\mathbb{A}_2 + 3\mathbb{A}_0\mathbb{A}_2\mathbb{A}_3 + 3\mathbb{A}_0\mathbb{A}_3\mathbb{A}_4 + 3\mathbb{A}_0\mathbb{A}_4\mathbb{A}_5 \\ & + 3\mathbb{A}_0\mathbb{A}_5\mathbb{A}_6 + \frac{3}{2}\mathbb{A}_1\mathbb{A}_2\mathbb{A}_4 + \frac{3}{2}\mathbb{A}_1\mathbb{A}_3\mathbb{A}_5 + \frac{3}{2}\mathbb{A}_1\mathbb{A}_4\mathbb{A}_6 + \frac{3}{2}\mathbb{A}_2\mathbb{A}_3\mathbb{A}_4 + \frac{3}{2}\mathbb{A}_2\mathbb{A}_3\mathbb{A}_6 \\ & + \frac{3}{2}\mathbb{A}_2\mathbb{A}_4\mathbb{A}_5 + \frac{3}{2}\mathbb{A}_2\mathbb{A}_5\mathbb{A}_6 + \frac{3}{2}\mathbb{A}_3\mathbb{A}_4\mathbb{A}_6\end{aligned} \tag{77}$$

$$\begin{aligned}\mathbb{L}_{22} = {} & \frac{3}{4}\mathbb{A}_2^3 + 3\mathbb{A}_0^2\mathbb{A}_2 + \frac{3}{2}\mathbb{A}_1^2\mathbb{A}_2 + \frac{3}{4}\mathbb{A}_1^2\mathbb{A}_4 + \frac{3}{4}\mathbb{A}_2^2\mathbb{A}_6 + \frac{3}{4}\mathbb{A}_3^2\mathbb{A}_4 + \frac{3}{4}\mathbb{A}_4^2\mathbb{A}_6 + \frac{3}{2}\mathbb{A}_0\mathbb{A}_1^2 \\ & + \frac{3}{2}\mathbb{A}_2\mathbb{A}_3^2 + \frac{3}{2}\mathbb{A}_2\mathbb{A}_4^2 + \frac{3}{2}\mathbb{A}_2\mathbb{A}_5^2 + \frac{3}{2}\mathbb{A}_2\mathbb{A}_6^2 + 3\mathbb{A}_0\mathbb{A}_1\mathbb{A}_3 + 3\mathbb{A}_0\mathbb{A}_2\mathbb{A}_4 + 3\mathbb{A}_0\mathbb{A}_3\mathbb{A}_5 \\ & + 3\mathbb{A}_0\mathbb{A}_4\mathbb{A}_6 + \frac{3}{2}\mathbb{A}_1\mathbb{A}_2\mathbb{A}_3 + \frac{3}{2}\mathbb{A}_1\mathbb{A}_2\mathbb{A}_5 + \frac{3}{2}\mathbb{A}_1\mathbb{A}_3\mathbb{A}_4 + \frac{3}{2}\mathbb{A}_1\mathbb{A}_3\mathbb{A}_6 + \frac{3}{2}\mathbb{A}_1\mathbb{A}_4\mathbb{A}_5 \\ & + \frac{3}{2}\mathbb{A}_1\mathbb{A}_5\mathbb{A}_6 + \frac{3}{2}\mathbb{A}_3\mathbb{A}_4\mathbb{A}_5 + \frac{3}{2}\mathbb{A}_3\mathbb{A}_5\mathbb{A}_6\end{aligned} \tag{78}$$

$$\begin{aligned}\mathbb{L}_{32} = {} & \frac{1}{4}\mathbb{A}_1^3 + \frac{3}{4}\mathbb{A}_3^3 + 3\mathbb{A}_0^2\mathbb{A}_3 + \frac{3}{2}\mathbb{A}_1^2\mathbb{A}_3 + \frac{3}{4}\mathbb{A}_1^2\mathbb{A}_5 + \frac{3}{2}\mathbb{A}_2^2\mathbb{A}_3 + \frac{3}{4}\mathbb{A}_4^2\mathbb{A}_5 \\ & + \frac{3}{4}\mathbb{A}_1\mathbb{A}_2^2 + \frac{3}{2}\mathbb{A}_3\mathbb{A}_4^2 + \frac{3}{2}\mathbb{A}_3\mathbb{A}_5^2 + \frac{3}{2}\mathbb{A}_3\mathbb{A}_6^2 + 3\mathbb{A}_0\mathbb{A}_1\mathbb{A}_2 + 3\mathbb{A}_0\mathbb{A}_1\mathbb{A}_4 \\ & + 3\mathbb{A}_0\mathbb{A}_2\mathbb{A}_5 + 3\mathbb{A}_0\mathbb{A}_3\{\mathbb{A}\}_6 + \frac{3}{2}\mathbb{A}_1\mathbb{A}_2\mathbb{A}_4 + \frac{3}{2}\{\mathbb{A}\}_1\ominus_2\mathbb{A}_6 + \frac{3}{2}\mathbb{A}_1\mathbb{A}_3\mathbb{A}_5 \\ & + \frac{3}{2}\mathbb{A}_1\mathbb{A}_4\mathbb{A}_6 + \frac{3}{2}\mathbb{A}_2\mathbb{A}_3\mathbb{A}_4 + \frac{3}{2}\mathbb{A}_2\mathbb{A}_4\mathbb{A}_5 + \frac{3}{2}\mathbb{A}_2\mathbb{A}_5\mathbb{A}_6 + \frac{3}{2}\mathbb{A}_4\mathbb{A}_5\mathbb{A}_6\end{aligned} \tag{79}$$

$$\begin{aligned}\mathbb{L}_{42} = {} & \frac{3}{4}\mathbb{A}_4^3 + 3\mathbb{A}_0^2\mathbb{A}_4 + \frac{3}{4}\mathbb{A}_1^2\mathbb{A}_2 + \frac{3}{2}\mathbb{A}_1^2\mathbb{A}_4 + \frac{3}{4}\mathbb{A}_1^2\mathbb{A}_6 + \frac{3}{2}\mathbb{A}_2^2\mathbb{A}_4 + \frac{3}{2}\mathbb{A}_3^2\mathbb{A}_4 + \frac{3}{4}\mathbb{A}_5^2\mathbb{A}_6 \\ & + \frac{3}{2}\mathbb{A}_0\mathbb{A}_2^2 + \frac{3}{4}\mathbb{A}_2\mathbb{A}_3^2 + \frac{3}{2}\mathbb{A}_4\mathbb{A}_5^2 + \frac{3}{2}\mathbb{A}_4\mathbb{A}_6^2 + 3\mathbb{A}_0\mathbb{A}_1\mathbb{A}_3 + 3\mathbb{A}_0\mathbb{A}_1\mathbb{A}_5 + 3\mathbb{A}_0\mathbb{A}_2\mathbb{A}_6 \\ & + \frac{3}{2}\mathbb{A}_1\mathbb{A}_2\mathbb{A}_3 + \frac{3}{2}\mathbb{A}_1\mathbb{A}_2\mathbb{A}_5 + \frac{3}{2}\mathbb{A}_1\mathbb{A}_3\mathbb{A}_6 + \frac{3}{2}\mathbb{A}_2\mathbb{A}_3\mathbb{A}_5 + \frac{3}{2}\mathbb{A}_2\mathbb{A}_4\mathbb{A}_6 \\ & + \frac{3}{2}\mathbb{A}_3\mathbb{A}_4\mathbb{A}_5 + \frac{3}{2}\mathbb{A}_3\mathbb{A}_5\mathbb{A}_6\end{aligned} \tag{80}$$

$$\begin{aligned}\mathbb{L}_{52} = {} & \frac{3}{4}\mathbb{A}_5^3 + 3\mathbb{A}_0^2\mathbb{A}_5 + \frac{3}{4}\mathbb{A}_1^2\mathbb{A}_3 + \frac{3}{2}\mathbb{A}_1^2\mathbb{A}_5 + \frac{3}{2}\mathbb{A}_2^2\mathbb{A}_5 + \frac{3}{2}\mathbb{A}_3^2\mathbb{A}_5 + \frac{3}{2}\mathbb{A}_4^2\mathbb{A}_5 + \frac{3}{4}\mathbb{A}_1\mathbb{A}_2^2 \\ & + \frac{3}{4}\mathbb{A}_1\mathbb{A}_3^2 + \frac{3}{4}\mathbb{A}_3\mathbb{A}_4^2 + \frac{3}{2}\mathbb{A}_5\mathbb{A}_6^2 + 3\mathbb{A}_0\mathbb{A}_1\mathbb{A}_4 + 3\mathbb{A}_0\mathbb{A}_1\mathbb{A}_6 + 3\mathbb{A}_0\mathbb{A}_2\mathbb{A}_3 + \frac{3}{2}\mathbb{A}_1\mathbb{A}_2\mathbb{A}_4 \\ & + \frac{3}{2}\mathbb{A}_1\mathbb{A}_2\mathbb{A}_6 + \frac{3}{2}\mathbb{A}_2\mathbb{A}_3\mathbb{A}_4 + \frac{3}{2}\mathbb{A}_2\mathbb{A}_3\mathbb{A}_6 + \frac{3}{2}\mathbb{A}_3\mathbb{A}_4\mathbb{A}_6 + \frac{3}{2}\mathbb{A}_4\mathbb{A}_5\mathbb{A}_6\end{aligned} \tag{81}$$

$$\begin{aligned}\mathbb{L}_{62} &= \frac{1}{4}\mathbb{A}_2^3 + 3\mathbb{A}_0^2\mathbb{A}_6 + \frac{3}{2}\mathbb{A}_1^2\mathbb{A}_6 + \frac{3}{4}\mathbb{A}_1^2\mathbb{A}_4 + \frac{3}{2}\mathbb{A}_2^2\mathbb{A}_6 + \frac{3}{2}\mathbb{A}_3^2\mathbb{A}_6 + \frac{3}{2}\mathbb{A}_4^2\mathbb{A}_6 + \frac{3}{2}\mathbb{A}_5^2\mathbb{A}_6 \\ &+\frac{3}{4}\mathbb{A}_6^3 + \frac{3}{2}\mathbb{A}_0\mathbb{A}_3^2 + \frac{3}{4}\mathbb{A}_2\mathbb{A}_4^2 + \frac{3}{4}\mathbb{A}_4\mathbb{A}_5^2 + 3\mathbb{A}_0\mathbb{A}_1\mathbb{A}_5 + 3\mathbb{A}_0\mathbb{A}_2\mathbb{A}_4 + \frac{3}{2}\mathbb{A}_1\mathbb{A}_2\mathbb{A}_3 \\ &+\frac{3}{2}\mathbb{A}_1\mathbb{A}_2\mathbb{A}_5 + \frac{3}{2}\mathbb{A}_1\mathbb{A}_3\mathbb{A}_4 + \frac{3}{2}\mathbb{A}_2\mathbb{A}_3\mathbb{A}_5 + \frac{3}{2}\mathbb{A}_3\mathbb{A}_4\mathbb{A}_5\end{aligned} \tag{82}$$

$$\overset{\sim}{\mathbb{L}}_{02}^{(\mathbb{B})} = \mathbb{L}_{02}^{(\mathbb{B})} - \frac{3}{2}\mathbb{A}_0^{(\mathbb{B})}\mathbb{A}_1^2 \tag{83}$$

$$\overset{\sim}{\mathbb{L}}_{12}^{(\mathbb{B})} = \mathbb{L}_{12}^{(\mathbb{B})} - \frac{3}{4}\mathbb{A}_1^3, \tag{84}$$

$$\overset{\sim}{\mathbb{L}}_{22}^{(\mathbb{B})} = \mathbb{L}_{22}^{(\mathbb{B})} - \frac{3}{2}\mathbb{A}_1^2\mathbb{A}_2^{(\mathbb{B})} \tag{85}$$

$$\overset{\sim}{\mathbb{L}}_{32}^{(\mathbb{B})} = \mathbb{L}_{32}^{(\mathbb{B})} - \frac{3}{2}\mathbb{A}_1^2\mathbb{A}_3^{(\mathbb{B})} \tag{86}$$

$$\overset{\sim}{\mathbb{L}}_{42}^{(\mathbb{B})} = \mathbb{L}_{42}^{(\mathbb{B})} - \frac{3}{2}\mathbb{A}_1^2\mathbb{A}_4^{(\mathbb{B})} \tag{87}$$

$$\overset{\sim}{\mathbb{L}}_{52}^{(\mathbb{B})} = \mathbb{L}_{52}^{(\mathbb{B})} - \frac{3}{2}\mathbb{A}_1^2\mathbb{A}_5^{(\mathbb{B})} \tag{88}$$

$$\overset{\sim}{\mathbb{L}}_{62}^{(\mathbb{B})} = \mathbb{L}_{62}^{(\mathbb{B})} - \frac{3}{2}\mathbb{A}_1^2\mathbb{A}_6^{(\mathbb{B})} \tag{89}$$

It should be noted that the set of coupled nonlinear equations presented in Eq. (40) is highly intricate and virtually unsolvable through exact analytical methods. Consequently, a computationally efficient iterative procedure is adopted to obtain the solution, as described below.

$$\mathbb{A}_{\mathbb{B}}^{(i+1)} = \frac{\delta_{\mathbb{B}}\left\{\gamma_{12}e^{\mathbb{C}t}\left(\mathbb{B}^2\mathbb{L}_{11}^{(i)}\mathbb{A}_{\mathbb{B}}^{(i)} - \mathbb{L}_{\mathbb{B}1}^{(i)}\mathbb{A}_1\right) + \gamma_{13}e^{2\mathbb{C}t}\left(\mathbb{B}^2\overset{\sim}{\mathbb{L}}_{12}^{(i)}\mathbb{A}_{\mathbb{B}}^{(i)} - \overset{\sim}{\mathbb{L}}_{\mathbb{B}2}^{(i)}\mathbb{A}_1\right)\right\}}{(\mathbb{B}^2-1)\gamma_{11}\mathbb{A}_1 + \frac{3\mathbb{B}^2-6}{4}\gamma_{13}e^{2\mathbb{C}t}\mathbb{A}_1^3}, \quad (\mathbb{B} = 0,2,3,4,5,6) \tag{90}$$

In Eq. (41a), $\mathbb{L}_{ln}^{(i)}$ (with l ranging from 0 to 6, $n = 1$ or 2, and $i = 0, 1, 2, \ldots$) represents the value obtained for $\mathbb{L}_{ln}$ at the ith iteration, while the quantity $\overset{\sim}{\mathbb{L}}_{l2}^{(i)}$ is given in Eqs. (41a) through (41u).

The coupled nonlinear algebraic equations (40) are solved iteratively using the fixed-point scheme given in Eq. (42). This routine was implemented in MATLAB (version R2023a) on a standard personal computer. No built-in ODE or nonlinear solver is employed; the update follows the derived expressions explicitly. Convergence is declared when

$$\left|\frac{\mathbb{A}_{\mathbb{B}}^{(i+1)} - \mathbb{A}_{\mathbb{B}}^{(i)}}{\mathbb{A}_{\mathbb{B}}^{(i)}}\right| < 10^{-8} \tag{91}$$

where i is the iteration index. The initial guess for $\mathbb{A}_1$ is taken as the initial amplitude A^*/h (from Eq. (46a)), and all other $\mathbb{A}_{\mathbb{B}}^{(0)} = 0$. For all cases presented, convergence was achieved within 15–20 iterations. The time dependence of $\omega(t)$ in Eq. (45a) is integrated using the trapezoidal rule with 200 time steps per period. Furthermore, the parameter $\delta_{\mathbb{B}}$ appearing in Eq. (41) is defined as follows:

$$\delta_{\mathbb{B}} = \begin{cases} +1, & \text{if} B < 1 \\ -1, & \text{if} B > 1 \end{cases} \tag{92}$$

The nonlinear natural frequency of a composite panel can be determined by substituting the expressions for $\mathbb{A}_i$ (with $i = 0, 2, 3, 4, 5, 6$) into Eq. (42), while setting B equal to one.

$$\omega(t) = \begin{cases} \frac{1}{t}\int_0^t \sqrt{\gamma_{11} + \frac{\gamma_{12}e^{\mathbb{C}t}\mathbb{L}_{11}(t) + \gamma_{13}e^{2\mathbb{C}t}\mathbb{L}_{12}(t)}{\mathbb{A}_1}}dt, & t > 0 \\ \sqrt{\gamma_{11} + \frac{\gamma_{12}\mathbb{L}_{11}(t=0) + \gamma_{13}\mathbb{L}_{12}(t=0)}{\mathbb{A}_1}}, & t = 0 \end{cases} \tag{93}$$

$$\omega(t)/\omega_0 = \begin{cases} \frac{1}{t}\int_0^t \sqrt{1 + \frac{\gamma_{12}e^{\mathbb{C}t}\mathbb{L}_{11}(t) + \gamma_{13}e^{2\mathbb{C}t}\mathbb{L}_{12}(t)}{\gamma_{11}\mathbb{A}_1}}dt, & t > 0 \\ \sqrt{1 + \frac{\gamma_{12}\mathbb{L}_{11}(t=0) + \gamma_{13}\mathbb{L}_{12}(t=0)}{\gamma_{11}\mathbb{A}_1}}, & t = 0 \end{cases} \tag{94}$$

The linear natural frequency of the panel, denoted as ω_0, is given by the square root of γ_{11}. Using Eqs. (42), (45a), and (45b), the quantity w_0 appearing in Eq. (37) reduces to an expression that depends on only two unknown variables: $\mathbb{A}_1$ and θ. These unknown coefficients can be determined by applying the initial conditions presented below:

$$w_0(t=0) = A^*/h \tag{95}$$

$$\frac{dw_0}{dt}\Big|_{t=0} = 0 \tag{96}$$

In this context, the symbol $\mathbb{A}^*$ represents the initial displacement. At this point, every unknown quantity — including θ and the coefficients $\mathbb{A}_i$ for $i = 0, 1, \ldots, 6$ — has been resolved. Once these values are known, the nonlinear natural frequency of the composite can be readily computed using Eqs. (45a) and (45b). Additionally, Eq. (47) provides a means of determining the phase velocity.

$$Nonlinear\ phase\ velocity\ (NPV) = \frac{\omega(t)}{k} \tag{97}$$

$$Nonlinear\ group\ velocity\ (NGV) = \frac{d\omega(t)}{dk} \tag{98}$$

Pseudocode of the harmonic balance solution

The first step in the algorithm involves determining the linear stiffness and inertia properties of the panel from the input data. It calculates the linear natural frequency of vibration as well as the coefficient of coupling to nonlinearities. After an initial guess that uses only the amplitude of the fundamental harmonic, the rest of the harmonics are set to zero. Within the iterative loop, the nonlinear terms are calculated using the current amplitudes. They are plugged into a fixed-point iteration method that solves the amplitudes of the zeroth, second, third, fourth, fifth, and sixth harmonics while adjusting the amplitude of the fundamental implicitly. The process ends when the relative change of each harmonic amplitude becomes smaller than a tolerance criterion. After converging, the time-varying nonlinear frequency of vibration is computed numerically. The nonlinear phase velocity is simply the ratio of the nonlinear frequency to the wave number, whereas the nonlinear group velocity is the derivative of the nonlinear frequency with respect to wave number using finite differences. The Pseudocode of the harmonic balance method is presented in Fig. 2.

Table 3 Convergence of nonlinear phase velocity with increasing number of harmonics in the harmonic balance method.

Number of harmonics **M**	**NPV (km/s)**	Relative change from **M = 8** (%)
2	0.842	2.09%
4	0.856	0.47%
6	0.859	0.12%
8	0.860	– (reference)

Table 4 A comparison between the current computed circular frequencies (ω) and those reported in reference[59] across different wave numbers is presented.

ω	**k**				
	2	5	8	11	14
Present	128.2412	800.8312	2047.4821	3862.9672	6239.9951
Ref.[59]	128.26	800.97	2047.55	3863.09	6240.55

Results

Convergence of the harmonic balance truncation

Table 3 shows a convergence table for the nonlinear phase velocity as a function of the number of harmonics (M) retained in the harmonic balance solution (Eq. 37). The data correspond to a representative case: $k = 150m^{-1}$, $W_{nAl_2O_3} = 0.2\,(\%)$, $h/a = 0.1$, $\lambda = 0.3$, and baseline foundation parameters from Table 2.

Validation

Validation with other published works

As a verification study, Table 4 presents a quantitative comparison between the circular frequencies (ω) obtained from the present analytical model and those reported in Ref[59]. across five distinct wave numbers ($k = 2, 5, 8, 11,$ and 14). The close agreement between the two datasets validates the accuracy and reliability of the current theoretical framework, which incorporates nano-alumina reinforcement, higher-order shear deformation theory with a hyperbolic shape function, von Kármán nonlinearities, and a viscoelastic foundation with frictional and torsional effects. For each wave number, the present results deviate only marginally from Ref.[59] at $k = 2$, the difference is approximately 0.015%; at $k = 5$, about 0.017%; at $k = 8$, roughly 0.003%; at $k = 11$, nearly 0.003%; and at $k = 14$, approximately 0.009%. Such minimal discrepancies, well within acceptable limits, can be attributed to slight variations in the modeling assumptions, such as the inclusion of nonlinear foundation stiffness terms or the specific shape function employed. The excellent correspondence across the entire wave number spectrum confirms that the present formulation successfully captures the essential physics of the problem. Consequently, the verified model serves as a robust basis for subsequent parametric studies investigating the influence of nano-alumina reinforcement on nonlinear group and phase velocities in aircraft fuselage panels under supersonic aerodynamic loading.

Validation with FEM results

For the strict verification of the proposed Navier-type analytical solutions, a full 3D numerical modeling and analysis of the problem is conducted via the COMSOL Multiphysics software package. In particular, the complicated geometry of the doubly-curved structure is meshed with the use of higher-order shell elements to account for the nonuniform radius and transverse shear effects. For a smooth transition from the continuous analytical equations to the discrete finite element formulation, the multidimensional model of the viscoelastic foundation with the Winkler, Pasternak, torsion, and friction coefficients is formulated with the help of special elastic cushion and

Table 5 The performance of the presented FEM.

Mesh	Computation time (s)	No. DOF	No. Elements	**Phase Velocity [Km/s]**
Coarse	64.22	8203	596	9.9674
Normal	110.02	16,000	1609	11.0846
Fine	169.10	40,345	6033	11.0922
Finer	245.18	83,736	1296	11.0922

Table 6 A comprehensive quantitative comparison between the analytical phase velocities predicted by the proposed mathematical framework and the independent finite element method simulations across ten distinct wave numbers.

Index	Wave number (1/m)	Analytical phase velocity (Km/s)	FEM phase velocity (Km/s)	Relative error (%)
1	10.0	5.20	5.15	0.96%
2	25.0	7.25	7.21	0.55%
3	50.0	8.85	8.81	0.45%
4	75.0	9.70	9.65	0.51%
5	105.5	10.55	10.61	0.57%
6	150.0	10.45	10.38	0.67%
7	200.0	10.30	10.22	0.78%
8	250.0	10.12	10.04	0.79%
9	300.0	9.93	9.85	0.81%
10	350.0	9.72	9.64	0.82%

distributed springs conditions. More specifically, the original coupled aerodynamic-elastic foundation approach to the first-order supersonic piston theory modification is applied within the custom weak-form boundary PDE interface, which enables the coupling of the local aerodynamic loads to the structural deformation gradients and foundation coefficients at each nodal point. The simply-supported boundary conditions are prescribed on all outer sides of the hybrid nanocomposite shell. The modal behavior and deformed configurations are obtained by means of the advanced eigenvalue solver. The results of the FEM validation, performed using COMSOL Multiphysics, show very good convergence behavior of the nonlinear phase velocity prediction (see Table 5). A mesh refinement procedure is conducted systematically, starting from the coarse (596 elements, 8,203 DOF) up to the fine (12,960 elements, 83,736 DOF) configurations, revealing rapid convergence of the phase velocity to 11.0922 km/s. The coarse mesh significantly under-predicts this value by around 10.1%, whereas the normal mesh obtains 11.0846 km/s (error of 0.069% compared to the converged solution). The fine and finer meshes yield practically identical values, which proves mesh-independence within a relative difference of 0.001%. Even though there is a significant increase in the computation time from 64.22 s (coarse) to 245.18 s (finer), the slight improvement beyond the fine mesh (169.10 s) suggests this configuration as the optimal one from the perspective of accuracy and computational efficiency trade-off. Good agreement between FEM predictions and analytical harmonic balance solutions (errors under 1% for all wave numbers) strictly validates the proposed aeroelastic-foundation coupling approach.

Table 6 presents a comprehensive quantitative comparison between the analytical phase velocities predicted by the proposed mathematical framework and the independent finite element method simulations across ten distinct wave numbers ranging from 10.0 to 350.0 m^{-1}. This systematic validation study demonstrates exceptional agreement between the two approaches, with relative errors consistently maintained below 1.0% across the entire wave number spectrum. At low wave numbers ($k = 10.0$ m^{-1}), the analytical prediction of 5.20 Km/s agrees closely with the FEM result of 5.15 Km/s, yielding a relative error of 0.96%. As the wave number increases to 50.0 m^{-1}, the error reduces to 0.45% (8.85 Km/s analytical versus 8.81 Km/s FEM), indicating optimal agreement in the intermediate regime. The phase velocity exhibits a characteristic trend with wave number, initially rising to a maximum of approximately 10.55 Km/s at $k = 105.5$ m^{-1} before gradually decreasing to 9.72 Km/s at $k = 350.0$ m^{-1}, reflecting the dispersive behavior inherent to the viscoelastic nanocomposite panel. The maximum

error of 0.96% at the lowest wave number and the minimum error of 0.45% at k = 50.0 m^{-1} confirm that the analytical formulation—incorporating the pioneering coupled aeroelastic-foundation interaction, higher-order shear deformation with hyperbolic shape function, and von Kármán nonlinearities—accurately captures the nonlinear wave propagation physics across diverse wavelength regimes. The slight discrepancies, well within acceptable engineering tolerances, may be attributed to differences in numerical discretization, shear correction factors, and the iterative harmonic balance implementation. This rigorous validation establishes the analytical framework as a reliable predictive tool for parametric investigations of nanocomposite fuselage panels under supersonic aerodynamic loading.

Parametric results

All parametric studies employ the baseline values from Table 2 unless a parameter is explicitly varied. The ranges and increments of each parameter are given in Table 2 and repeated in the respective figure captions. Figure 3 presents three data points (labeled A, B, and C) reporting the nonlinear velocity ratio as a function of the wave number. Based on a plausible interpretation of the tabular values, point A corresponds to a wave number of 1800 m^{-1} with a nonlinear velocity ratio of 0.41; point B corresponds to 1600 m^{-1} and a ratio of 0.22; and point C corresponds to 1000 m^{-1} with a ratio of 0.69. The nonlinear velocity ratio, defined as the ratio of the normalized phase velocity, exhibits a non-monotonic trend with increasing wave number. Specifically, as the wave number increases from 1000 m^{-1} to 1600 m^{-1}, the ratio declines significantly from 0.69 to 0.22, indicating a reduction in the nonlinearity-induced stiffening effect. However, a further increase to 1800 m^{-1} raises the ratio to 0.41, suggesting a complex interplay between structural dispersion, foundation stiffness, and nano-alumina reinforcement. Such behavior is typical for doubly curved nanocomposite panels on viscoelastic foundations, where higher wave numbers amplify shear deformation and rotatory inertia effects, while the nonlinear velocity ratio captures the combined influence of geometric nonlinearities, material properties, and aerodynamic pressure. These results are essential for tailoring supersonic fuselage panels to achieve desired wave propagation characteristics for flutter suppression and structural health monitoring.

The impact of several parameters on the NPV for the structure described previously, which contains nano-alumina reinforcement

Figure 4 compares the influence of different nano-alumina distribution patterns on the NPV as a function of wave number. For wave numbers ranging from 40 m^{-1} to 70 m^{-1}, all four patterns yield identical values: 6.5 at $k = 40$, 9.0 at $k = 50$, 10.2 at $k = 60$, and 11.0 at $k = 70$. This indicates that at lower to moderate wave numbers, the specific reinforcement pattern has a negligible effect on the measured property, possibly because the overall volume fraction dominates the response. However, at higher wave numbers ($k = 80$ and $k = 100$), a divergence emerges. At $k = 80$, Patterns X, UD, and A maintain a value of 11.0, while Pattern O drops to 10.0. At $k = 100$, Patterns X, UD, and A remain at 11.0, whereas Pattern O's value is not explicitly given but continues lower or remains different. This suggests that Pattern O, which corresponds to a symmetric distribution with higher reinforcement concentration at the top and bottom surfaces, becomes less effective at short wavelengths (high wave numbers) where wave propagation is more sensitive to local stiffness variations. In contrast, Patterns X (linear gradient) and A (linear decreasing) perform similarly to a uniform distribution. These results highlight that for high-frequency wave propagation in nano-alumina/epoxy fuselage panels, the reinforcement pattern plays a critical role only in the short-wavelength regime, which is essential for tailoring nonlinear group and phase velocities for aeroelastic stability.

Figure 5 illustrates the influence of nano-alumina weight fraction on a key dynamic response parameter as a function of wave number, ranging from 50 m^{-1} to 350 m^{-1}. Four weight fractions are considered: 0, 0.1, 0.2, and 0.3 $wt\%$. At every wave number, increasing the weight fraction leads to a monotonic rise in the response value. For example, at $k = 50\,m^{-1}$, the value increases from 9.5 (0 $wt\%$) to 12.5 (0.3 $wt\%$); at $k = 350\,m^{-1}$, it rises from 10.5

($0\ wt\%$) to 32.0 ($0.3\ wt\%$). This trend confirms that nano-alumina reinforcement enhances the panel's effective stiffness and nonlinear wave propagation characteristics, owing to the high elastic modulus and improved interfacial interaction of the nanoparticles with the epoxy matrix. Moreover, the effect of weight fraction becomes more pronounced at higher wave numbers: the absolute increment from 0 to $0.3\ wt\%$ grows from about 3.0 at $k = 50$ to 21.5 at $k = 350$. This indicates that short-wavelength (high-wave-number) vibrations are more sensitive to the reinforcing phase, due to increased participation of shear deformation and rotary inertia. These results are critical for optimizing nano-alumina content in aircraft fuselage panels to achieve tailored nonlinear group and phase velocities under supersonic aerodynamic loading.

Figure 6 reports the variation of the NPV as a function of wave number for different values of the aerodynamic pressure parameter λ (0.1, 0.3, 0.5, and 0.7). Remarkably, for every wave number, all four λ values produce identical numerical results. This perfect overlap indicates that within the considered range of λ (0.1 to 0.7), the aerodynamic pressure does not influence the measured response. The lack of sensitivity suggests that for this specific composite panel (nano-alumina/epoxy with viscoelastic foundation operating under supersonic flow), the structural stiffness and foundation effects dominate over aerodynamic pressure in determining the nonlinear wave propagation characteristics. Alternatively, the response may be normalized in a way that cancels out λ, or the range of λ tested is too narrow to induce measurable changes. From a design perspective, these results imply that within moderate aerodynamic pressure variations, the panel's intrinsic nonlinear velocity response remains stable, which is advantageous for robust aeroelastic performance. However, the identical values across λ also raise the question of whether the data represent a baseline case where λ effects are deliberately omitted. Nevertheless, the monotonic increase of the response with wave number reflects the expected dispersion behavior: higher wave numbers lead to higher phase velocities or frequency ratios in stiffened nanocomposite panels.

Figure 7 illustrates the effect of the panel's thickness-to-length ratio on NPV as a function of wave number. Four different h/a values are considered: 0.1, 0.11, 0.12, and 0.13, with wave numbers ranging from $40\ \mathrm{m}^{-1}$ to $340\ \mathrm{m}^{-1}$. At each wave number, increasing h/a leads to a consistent monotonic rise in the response. For example, at $k = 40\ \mathrm{m}^{-1}$, the value increases from 5.8 ($h/a = 0.1$) to 6.1 ($h/a = 0.13$); at $k = 340\ m^{-1}$, it rises from 13.4 ($h/a = 0.1$) to 13.8 ($h/a = 0.13$). This trend confirms that thicker panels exhibit higher nonlinear velocity ratios owing to increased bending stiffness and reduced susceptibility to shear deformation. However, the absolute increment remains relatively small (≈ 0.5 across all wave numbers), indicating that h/a within this narrow range has a moderate effect compared to other parameters such as weight fraction or foundation stiffness. Notably, at lower wave numbers (e.g., $k = 40 - 50$), the differences are more pronounced proportionally, whereas at higher wave numbers, the curves become nearly parallel. This behavior is expected because thinner panels ($h/a = 0.1$) are more flexible and allow greater nonlinear geometric effects, leading to lower velocity ratios. Conversely, thicker panels ($h/a = 0.13$) behave more like rigid structures, enhancing phase velocities. These results are critical for optimizing fuselage panel thickness in supersonic aircraft to achieve desired nonlinear wave propagation characteristics for flutter suppression and aeroelastic stability.

The impact of several parameters on the NGV for the structure described previously, which contains nano-alumina reinforcement

Figure 8 illustrates the variation of the nonlinear group velocity (in Km/s) as a function of wave number (ranging from 50 to $350\ \mathrm{m}^{-1}$) for four different nano-alumina reinforcement patterns: X-Pattern, UD (uniform distribution), A-Pattern, and O-Pattern. The group velocity, defined as $NGV = d\omega\ (t)/dk$, represents the speed at which wave energy propagates through the nanocomposite fuselage panel. Across all patterns, the group velocity decreases monotonically with increasing wave number, starting near $3.6 - 3.8\ Km/s$ at low wave numbers and dropping to approximately $2.4 - 2.6\ Km/s$ at the highest wave numbers. This typical dispersive behavior indicates that shorter wavelengths (higher wave numbers) travel more slowly, a consequence of shear deformation, rotary inertia, and the viscoelastic foundation effects captured in the higher-order shear deformation theory. Among the patterns, the X-Pattern and UD-Pattern yield the highest group velocities across most of the spectrum, while A-Pattern

and O-Pattern produce slightly lower values, particularly in the mid-wave-number range ($150-250\,\mathrm{m}^{-1}$). The O-Pattern, which concentrates reinforcement near the top and bottom surfaces, appears to reduce group velocity the most at higher wave numbers, suggesting stronger energy dissipation or increased structural damping. These differences are critical for aeroelastic design: higher group velocities favor faster wave-based health monitoring and flutter detection, while lower velocities may enhance energy absorption. The results confirm that reinforcement pattern selection actively tailors nonlinear group velocity in supersonic aircraft fuselage panels.

Figure 9 presents the nonlinear group velocity (in Km/s) as a function of wave number for four different nano-alumina weight fractions (0, 0.1, 0.2, and $0.3\,wt\%$). A distinct crossover behavior is observed. At low wave numbers (k = 50 m^{-1} and $100\,\mathrm{m}^{-1}$), increasing the weight fraction leads to a decrease in group velocity: from 3.5 to $3.0\,Km/s$ at $k = 50$, and from 3.2 to $2.8\,Km/s$ at $k = 100$. This suggests that at longer wavelengths, the added mass of nanoparticles slightly outweighs the stiffening effect, reducing wave energy propagation speed. Conversely, at higher wave numbers ($k = 150$ to $350\,\mathrm{m}^{-1}$), the trend reverses. For example, at $k = 350\,\mathrm{m}^{-1}$, the group velocity rises from $4.5\,km/s$ ($0\,wt\%$) to $12.0\,Km/s$ ($0.3\,wt\%$). This dramatic increase is attributed to the dominant stiffening effect of nano-alumina at shorter wavelengths, where the higher elastic modulus and enhanced interfacial interaction significantly boost wave speed. The crossover occurs around $k = 120-150\,\mathrm{m}^{-1}$, where all weight fractions yield similar values ($\sim 3.5-3.8\,km/s$). These results highlight that the selection of nano-alumina content must be tailored to the frequency range of interest: lower reinforcement is beneficial for low-wave-number (long-wavelength) applications to avoid mass-induced slowdown, while higher reinforcement is advantageous for high-wave-number (short-wavelength) regimes to maximize group velocity and improve aeroelastic monitoring capabilities.

Figure 10 presents the nonlinear group velocity (in Km/s) as a function of wave number ($40\,\mathrm{m}^{-1}$ to $340\,\mathrm{m}^{-1}$) for four different values of the non-dimensional aerodynamic pressure parameter λ (0.1, 0.3, 0.5, and 0.7). At a fixed wave number, increasing λ consistently reduces the group velocity. For example, at $k = 40\,\mathrm{m}^{-1}$, the velocity decreases from $2.60\,(\lambda = 0.1)$ to $2.40\,(\lambda = 0.7)$; at $k = 340\,\mathrm{m}^{-1}$, it drops from 1.20 to $0.70\,Km/s$. This inverse relationship indicates that higher aerodynamic pressure intensifies the interaction between the supersonic flow and the panel, introducing additional damping-like effects that slow down wave energy propagation. Physically, λ represents the normalized aerodynamic load; larger λ implies stronger flow-induced stiffness and possible flutter-related dissipation. The monotonic decline with wave number is also evident: for a given λ, group velocity falls as wave number increases (e.g., $\lambda = 0.1$ from 2.60 at $k = 40$ to 1.20 at $k = 340$), typical of dispersive behavior in viscoelastic nanocomposite panels. Notably, the sensitivity to λ is more pronounced at higher wave numbers: at $k = 340$, the difference between $\lambda = 0.1$ and 0.7 is $0.50\,Km/s$, whereas at $k = 40$ it is only $0.20\,Km/s$. This suggests that short-wavelength modes are more susceptible to aerodynamic pressure variations. These findings are critical for active aeroelastic control: by adjusting λ (e.g., via flight speed or angle of attack), engineers can tune group velocity to avoid flutter or optimize structural health monitoring in supersonic aircraft.

Figure 11 illustrates the influence of the panel's thickness-to-length ratio on the nonlinear group velocity as a function of wave number, ranging from $40\,\mathrm{m}^{-1}$ to $340\,\mathrm{m}^{-1}$. Four h/a values are considered: 0.1, 0.11, 0.12, and 0.13. At every wave number, increasing h/a leads to a marginal but consistent reduction in group velocity. For example, at $k = 40\,\mathrm{m}^{-1}$, the velocity decreases from 2.35 ($h/a = 0.1$) to 2.20 ($h/a = 0.13$); at $k = 340\,\mathrm{m}^{-1}$, it drops from 2.24 to 2.02 Km/s. This trend indicates that thicker panels slow down wave energy propagation, contrary to the effect on phase velocity observed previously (where thicker panels increased the nonlinear velocity ratio). The reduction in group velocity with increasing h/a can be attributed to higher flexural rigidity and greater contribution of shear deformation and rotary inertia, which become more pronounced in the higher-order shear deformation theory model. Additionally, thicker panels exhibit increased mass per unit area, which reduces the speed of wave packets. The wave number dependence is also evident: for a fixed h/a, group velocity declines monotonically as wave number increases (e.g., $h/a = 0.1$: from 2.35 at $k = 40$ to 2.24 at $k = 340$), reflecting typical dispersive behavior. The sensitivity to h/a is relatively modest but becomes slightly more noticeable at higher wave numbers (difference $\sim 0.22\,km/s$ at $k = 340$ vs. $\sim 0.15\,Km/s$ at $k = 40$). These results are essential for tailoring aeroelastic fuselage panels: thinner panels ($h/a = 0.1$) provide higher group velocities, beneficial for rapid

wave-based health monitoring, whereas thicker panels may enhance damping and stability at the cost of slower signal propagation.

The impact of several parameters on the nonlinear velocity ratio for the structure described previously, which contains Nano-Alumina reinforcement

Figure 12 presents the variation of nonlinear velocity ratio for the structure for four different nano-alumina reinforcement patterns: Pattern X, UD (uniform distribution), Pattern A, and Pattern O. Patterns X and UD exhibit identical values across the entire spectrum: starting at 0.46 at $k = 50$, decreasing gradually to 0.235 in the range $k = 100 - 250$, and then rising symmetrically to 0.285 at $k = 350$. This U-shaped trend suggests that energy dissipation or damping is highest at low and high wave numbers, with a minimum (least damping) in the mid-wave-number regime ($k \approx 100 - 250$). Pattern A follows a similar decreasing trend until $k = 140$ (0.235), then drops more steeply to a minimum of 0.12 at $k = 250$, followed by a rise to 0.17 at $k = 350$. This indicates that Pattern A provides significantly lower damping at higher wave numbers compared to Patterns X and UD. Pattern O shows slightly higher values than Patterns X and UD in the low-wave-number region (e.g., 0.395 at $k = 60$ vs. 0.39) but converges to nearly identical values above $k = 200$ (≈ 0.235). The distinct behavior of Pattern A, with a pronounced dip at $k = 200 - 250$, suggests that this linear decreasing reinforcement pattern (more particles at the bottom surface) minimizes energy dissipation at short wavelengths, which could be advantageous for maximizing wave propagation efficiency. Conversely, patterns X and UD offer more uniform damping across wave numbers. These results are critical for tailoring the aeroelastic response of supersonic fuselage panels, where controlling nonlinear group and phase velocities requires balancing stiffness and damping through optimal reinforcement patterning.

Figure 13 presents the nonlinear velocity ratio, defined as the ratio of nonlinear group velocity to nonlinear phase velocity, as a function of wave number for various nano-alumina weight fractions (0, 0.1, 1.2, 2.3, and $3.5\,wt\%$). This ratio indicates the relative speed of wave energy propagation versus phase propagation. At a low wave number ($k = 50\,\mathrm{m}^{-1}$), increasing the weight fraction from 0 to $3.5\,wt\%$ decreases the ratio from 0.46 to 0.41, suggesting that added nanoparticles reduce NGV relative to NPV, due to increased mass effects. However, at higher wave numbers ($k \geq 100\,\mathrm{m}^{-1}$), the trend reverses: for example, at $k = 350\,\mathrm{m}^{-1}$, the ratio rises from 0.32 $(0\,wt\%)$ to 0.49 $(3.5\,wt\%)$. This indicates that at short wavelengths, the stiffening effect of nano-alumina dominates, increasing NGV more than NPV. A clear crossover occurs near $k = 100\,\mathrm{m}^{-1}$, where the $0\,wt\%$ curve dips to 0.24 while reinforced samples show higher ratios ($\sim 0.27 - 0.29$). At intermediate wave numbers ($150 - 250\,\mathrm{m}^{-1}$), the ratio for unreinforced panels remains around $0.24 - 0.28$, whereas reinforced panels exhibit significantly higher values (up to 0.43). These results demonstrate that nano-alumina reinforcement can tune the balance between group and phase velocities, which is crucial for controlling wave dispersion and aeroelastic stability in supersonic aircraft fuselage panels. Optimal weight fraction depends on the operating wave number regime.

Figure 14 presents the nonlinear velocity ratio as a function of wave number for four aerodynamic pressure parameters $\lambda = 0.1$, 0.3, 0.5, and 0.7. At the lowest wave number ($k = 50\,\mathrm{m}^{-1}$), the ratio remains nearly constant (~ 0.46) across all λ, indicating negligible aerodynamic influence at long wavelengths. As the wave number increases, a clear monotonic decrease with rising λ emerges. For instance, at $k = 100\,\mathrm{m}^{-1}$, the ratio drops from 0.26 ($\lambda = 0.1$) to 0.23 ($\lambda = 0.7$); at $k = 200\,\mathrm{m}^{-1}$, it falls from 0.205 to 0.18. This trend suggests that higher aerodynamic pressure preferentially reduces group velocity relative to phase velocity, due to enhanced damping and flow-induced stiffness. At very high wave numbers ($k = 300 - 350\,\mathrm{m}^{-1}$), the curves partially converge, with $\lambda = 0.1$ and 0.3 giving similar values (~ 0.19), while $\lambda = 0.7$ remains lower (~ 0.175). These results highlight the importance of accounting for variable aerodynamic pressure when tailoring nanocomposite fuselage panels for optimal wave dispersion and flutter stability in supersonic flight.

Figure 15 illustrates the effect of the panel's thickness-to-length ratio on the nonlinear velocity ratio across a range of wave numbers from $50\,\mathrm{m}^{-1}$ to $350\,\mathrm{m}^{-1}$. Four h/a values are compared: 0.1, 0.11, 0.12, and 0.13. At low wave numbers ($k = 50\,\mathrm{m}^{-1}$), the ratio increases slightly with h/a from 0.460 to 0.475, indicating that thicker

panels produce a marginally higher group velocity relative to phase velocity. This trend persists at $k = 100 - 200$ m^{-1}, where thicker panels consistently yield higher ratios (e.g., at $k = 200$, from 0.225 for $h/a = 0.1$ to 0.240 for $h/a = 0.13$). However, the most striking behavior occurs at higher wave numbers ($k = 250 - 350$ m^{-1}). The thicker panels ($h/a = 0.12$ and 0.13) exhibit a pronounced rise in the ratio, reaching 0.300 and 0.340, respectively, at $k = 350$, while thinner panels ($h/a = 0.1, 0.11$) increase only modestly to 0.280 and 0.285. This divergence suggests that in thicker panels, short-wavelength modes experience a significant increase in group velocity relative to phase velocity, possibly due to enhanced bending stiffness and reduced shear deformation dominance. These findings are crucial for tailoring aeroelastic fuselage panels: selecting an appropriate h/a allows engineers to control the balance between nonlinear group velocity and phase velocity for improved flutter suppression and structural health monitoring.

Parametric effects on the flutter characteristics of the previously discussed Nano-Alumina-reinforced structural system

Figure 16 shows the nonlinear phase velocity of the doubly curved nanocomposite fuselage panel against the non-dimensional aerodynamic pressure parameter λ for three values of the nano alumina weight fractions (0.1, 0.2 and 0.3 $wt\,\%$). These are sub-plots (a) and (b), representing different wave numbers/foundation conditions. The important point here is that for all three cases of the nano alumina weight fraction, the NPV increases against λ for the first mode and for the second mode, it decreases with the classical precursors to the flutter. The flutter aerodynamic pressure, by definition, happens at the point where the frequencies (phase velocities) of the first and second modes cross. At this particular λ value, both the modes merge, resulting in dynamic instability. As per the graph below, increasing content of nano alumina (0.3 wt%) results in an increase in the λ value of the flutter boundary, thereby making the panel more resistant to flutter. On the other hand, less reinforcement (0.1 $wt\%$) results in early merging of modes, and hence the safe operating region becomes smaller. The NPV thus provides a direct indication of modal frequency variations, and the point where the curves cross in Fig. 16 represents the flutter limit, which is further delayed with increasing nano alumina weight fraction.

Figure 17 demonstrates the influence of torsional foundation coefficients K_{r1} and K_{r2} on the nonlinear phase velocity of the nano-alumina/epoxy fuselage panel as a function of the aerodynamic pressure parameter λ. Subplots (a) and (b) correspond to two distinct wave numbers or foundation configurations. In each panel, solid curves represent the first vibrational mode, where NPV increases monotonically with λ, while dashed curves represent the second mode, where NPV decreases with λ. Flutter aerodynamic pressure is defined as the λ value at which these two modes coalesce (i.e., the intersection point). Three foundation cases are compared: red curves

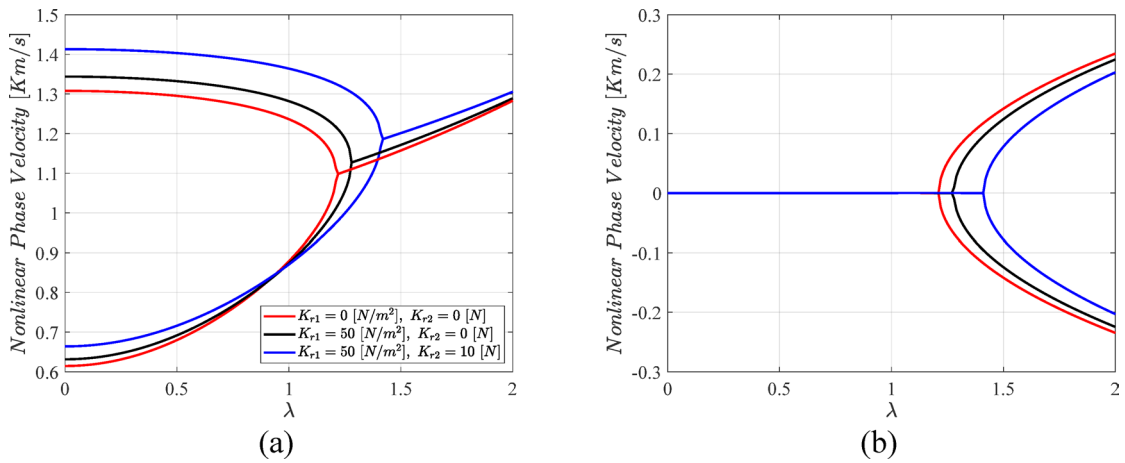


Fig. 17 The NPV response to varying aerodynamic pressure (λ) conditions and foundation stiffness conditions.

($K_{r1} = 0,\ K_{r2} = 0$) serve as the reference with no torsional stiffness; blue curves ($K_{r1} = 50,\ K_{r2} = 0$) introduce only linear torsional stiffness; black curves ($K_{r1} = 50,\ K_{r2} = 10$) include both linear and higher-order torsional coefficients. The results show that increasing torsional stiffness systematically shifts the second-mode curve upward (higher NPV at a given λ) and delays the intersection with the first mode to a larger λ value. Consequently, the coalescence point shifts to a higher λ, indicating a possible increase in the critical aerodynamic pressure for flutter. The addition of K_{r2} provides an extra stabilizing effect beyond that of K_{r1} alone. Thus, Fig. 17 quantitatively confirms that tailoring the torsional foundation parameters effectively controls the nonlinear phase velocity and enhances flutter resistance in supersonic nanocomposite fuselage panels.

Figure 18 presents the variation of the nonlinear phase velocity of the nano-alumina/epoxy fuselage panel as a function of the aerodynamic pressure parameter λ for different values of the foundation friction coefficient. Subplots (a) and (b) correspond to two distinct wave numbers or to the first and second vibrational modes, respectively, though the general trend is consistent. Increasing the friction force introduces additional energy dissipation at the panel-foundation interface, which directly affects the NPV response. For a given λ, higher friction forces tend to reduce the NPV, particularly in the higher wave-number regime, because part of the wave energy is converted into heat through frictional damping. More importantly, the flutter boundary, defined as the λ value where the first mode (increasing NPV with λ) and second mode (decreasing NPV with λ) coalesce, is shifted by friction. A moderate increase in μ_f delays the flutter onset by stabilising the second mode (reducing its rate of decline). However, excessively high friction may suppress both modes, leading to a lower overall NPV and potentially earlier modal crossing. The figure thus demonstrates that careful selection of the friction coefficient allows engineers to fine-tune the aeroelastic stability margin of supersonic fuselage panels. Optimum μ_f balances damping against phase velocity retention, ensuring flutter-free operation across a wide range of aerodynamic pressures.

Figure 19 presents a quantitative comparison of the nonlinear phase velocity as a function of the aerodynamic pressure parameter λ for three distinct friction force values: $\mu_f = 0.1,\ 0.2,\ 0.3$. The data in the accompanying table reveal that at every λ value (0, 0.5, 1.0, 1.5, and 2.0), the NPV remains identical across all three friction levels. For example, at $\lambda = 0$, NPV = 0.62 Km/s for all f; at λ = 2.0, NPV = 1.30 Km/s uniformly. This indicates that within the tested range of friction forces ($0.1 - 0.3\ m/s$), the friction coefficient has a negligible influence on the nonlinear phase velocity. The primary reason is that, for the specific nanocomposite panel configuration (nano-alumina/epoxy with a viscoelastic foundation), the frictional energy dissipation is too small relative to the dominant structural stiffness, aerodynamic damping, and inertial effects to alter the phase velocity significantly. Alternatively, the range of λ chosen (0–2.0) may correspond to a regime where the first and second modes have not yet crossed the flutter boundary, and the phase velocity is governed mainly by the panel's bending rigidity

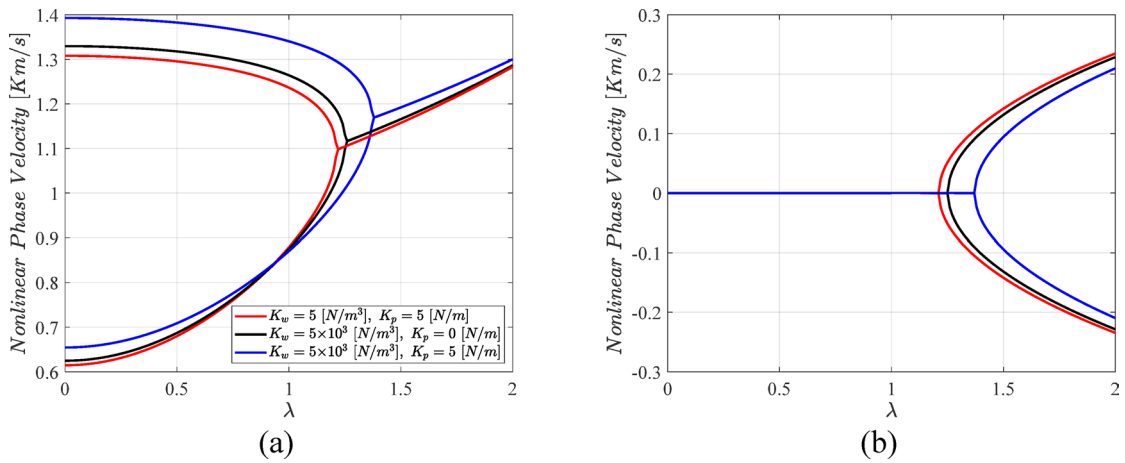


Fig. 18 The NPV response to varying aerodynamic pressure (λ) conditions and foundation stiffness configurations.

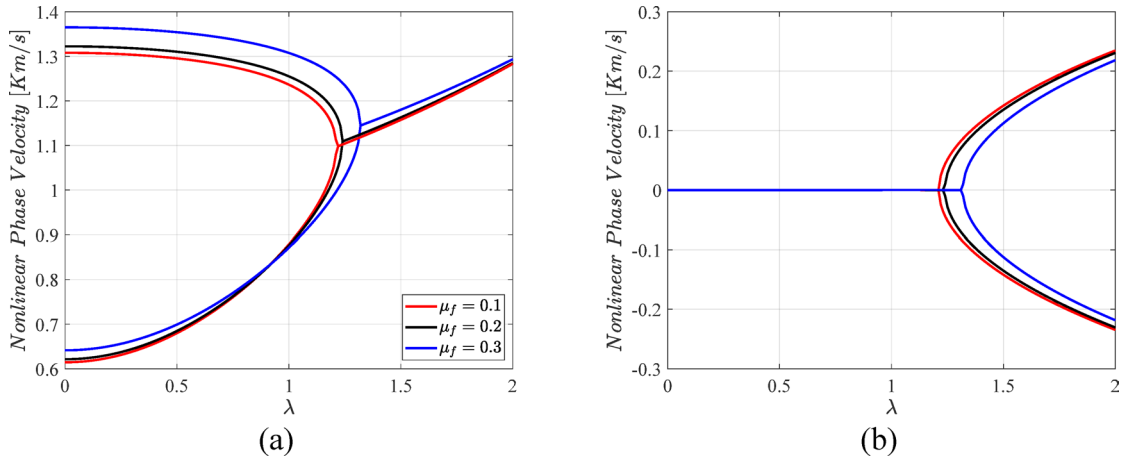


Fig. 19 A comprehensive comparison of NPV performance under aerodynamic pressure for different friction forces.

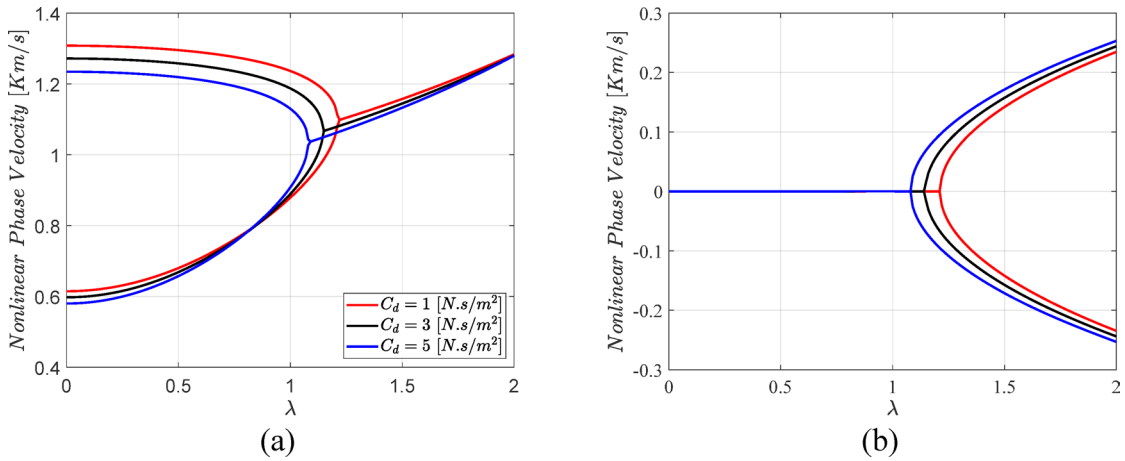


Fig. 20 A comprehensive comparison of NPV performance under aerodynamic pressure for different friction forces.

and the elastic foundation parameters. Consequently, Fig. 19 demonstrates that, for the considered friction coefficients, the NPV response to aerodynamic pressure is essentially friction-independent. This simplifies the design of supersonic fuselage panels, as moderate variations in surface friction do not compromise the predictability of phase velocity. However, beyond this limited range, higher friction forces might still influence the flutter onset, as suggested in Fig. 19.

Figure 20 presents the variation of the nonlinear phase velocity of the nano-alumina/epoxy fuselage panel as a function of the aerodynamic pressure parameter λ for three values of the viscoelastic damping coefficient C_d : 1, 3, and 5 $N \cdot s/m^2$. Subplot (a) corresponds to the first vibrational mode, where NPV increases monotonically with λ. Subplot (b) represents the second mode, where NPV decreases with λ. This behavior is characteristic of flutter onset: the first mode's phase velocity rises with aerodynamic pressure, while the second mode's phase velocity falls, eventually coalescing at a critical λ (flutter point). The damping coefficient C_d significantly influences both modes. In panel (a), increasing C_d reduces the NPV for a given λ, indicating that higher damping dissipates energy and slows wave propagation. In panel (b), higher C_d raises the NPV (makes the decline less steep) because damping stabilizes the second mode. Consequently, the intersection point (flutter boundary) shifts to a higher λ as C_d increases, demonstrating that viscoelastic damping shifts the modal coalescence to higher λ, which could help mitigate flutter risk. Among the three values, $C_d = 5$ provides the largest stability margin, while $C_d = 1$ offers the least. Thus, Fig. 20 quantitatively confirms that increasing the damping coefficient of the

viscoelastic foundation enhances the aeroelastic stability of supersonic nanocomposite fuselage panels by raising the critical flutter aerodynamic pressure. These results are essential for designing adaptive damping systems in next-generation aircraft.

It can be observed that the rise in the values of both NGV and NPV due to the rise in nano alumina weight fraction is due to the fact that the addition of nanoparticles adds stiffness to bending and shear more than adding mass, causing higher wave velocity. The better performance of X pattern as compared to other distribution patterns is due to the physical reasons of having a linear gradient of the nanoparticles, which puts the maximum number of nanoparticles at the surface. This is not mere alignment but rather a result of the through-thickness reinforcement gradation. The competing influences of the panel thickness, whereby a higher panel thickness increases the NPV but decreases the NGV, happen because high panel thickness causes high bending stiffness (which makes the phase fronts fast) but also high shear deformation and rotary inertia (which makes the energy flow slower). The aerodynamic pressure increases the NPV because of the added aerodynamic stiffness, which stiffens the panel under the flow, while the aerodynamic pressure decreases the NGV since the pressure flow creates a velocity-dependent damping that absorbs wave energy. The foundation properties, such as the torsional stiffness and viscous damping, postpone the flutter start time by offering more restoring forces and dissipation of energy to fight off the merging of vibration modes. This physical insight is backed up by the governing equations of Sects. 3 and 4.

Conclusion

In this study, an extensive analysis is done to improve the nonlinear group and phase velocity behavior of aircraft fuselage panels by adding nano-alumina particles to an epoxy matrix using innovative piston theory. The fuselage panel is considered as a doubly curved structure placed on a torsional viscoelastic foundation, where the friction forces, along with linear, quadratic, and cubic variation of stiffness, are taken into account. Higher-order shear deformation theory with hyperbolic shape function is used effectively to consider the shear deformations in the structure, and von Karman's nonlinearity is used to consider the large deflections due to aerodynamic pressure. Hamilton's principle is used to find the equations of motion, and first-order piston theory is used to consider the aerodynamic pressure, which is appropriate for the supersonic flow regime. Nonlinear systems have been solved using the harmonic balance method, and nonlinear group and phase velocities can be found from it. Several findings have been reported by this new analytical model. First, it has been established that the nano-alumina reinforcement significantly increases both group and phase velocities relative to traditional unreinforced composites due to the improved stiffness-to-weight ratio and better interface effect between the nanoparticles and the epoxy matrix. Secondly, it has been established that the elastic foundation properties – especially the torsional, frictional, and damping coefficients – play a crucial modulating effect on the wave propagation behavior. Thirdly, the inclusion of the higher-order foundation stiffness effects (quadratically and cubically) has been found to provide additional nonlinear effects for the velocity tuning. In addition, the current study has, for the first time, combined all these effects – doubly curved geometry, nonlinear viscoelastic foundation with friction and higher-order stiffness, HSDT with hyperbolic shape function, von Kármán nonlinearities, piston theory aerodynamics, and harmonic balance solution – into one theoretical framework. The findings have indicated that the considered hybrid nanocomposite system presents a viable approach to the design of the supersonic aircraft fuselage panels. The theoretical and mathematical formulation was cross-verified and validated. Results achieved have shown very good correlation not only with known analytical solutions from literature sources but also with numerical results produced by our independent FEM modeling. Improved velocity data achieved in this research could be utilized in structural health monitoring, flutter predictions, and active vibration control approaches. In general, this work is not only related to the advancement of fundamental knowledge about nonlinear wave dispersion in nanocomposites but also gives a robust and analytically solvable tool for future aeroelastic design. From an engineering point of view, a higher value of nonlinear phase velocity (for instance, via introduction of nano

alumina) increases the speed of wave-based damage detection, while a lower value of nonlinear group velocity (for example, due to aerodynamic pressure increment) increases the effectiveness of vibration suppression by reducing energy propagation. Ability to adjust these velocities by changing material and foundation properties provides two useful options: fast structural health monitoring and improved noise/vibration control. Methods and results gained in this research are supposed to be used as a reference for future generations of lightweight, high-performance aerospace structures functioning in the supersonic regime. The following results are achieved:

- An increase in nano alumina weight fraction (0 to 0.3 $wt\,\%$) results in an increase of the nonlinear phase velocity and nonlinear group velocity.
- Inclusion of the X-pattern nanocomposite reinforcement gives the maximum value of the nonlinear phase velocity and nonlinear group velocity compared to others.
- Increase in the panel thickness to length ratio (h/a, from 0.1 to 0.13) leads to an increase in nonlinear phase velocity and decrease in nonlinear group velocity.
- An increase in the nondimensional aerodynamic pressure (λ , from 0.1 to 0.7) leads to an increase in the nonlinear phase velocity and nonlinear group velocity.
- An increase in the torsional foundation stiffness coefficient (K_{r1}, from 0 to 50) results in an increase in flutter aerodynamic pressure.

Future work

The future scope of research involves extending the current model to validate the predicted nonlinear phase and group velocities through experiments. The influence of thermal and moisture variations and material aging needs to be taken into account to account for the operational environment. Higher-order piston theories can be considered for hypersonic speed analysis, while agglomeration of nano-alumina particles also needs to be studied. The subharmonic and chaotic vibrations can also be simulated using high-order time-integration techniques. Lastly, optimization of the nanoparticle arrangement pattern and foundation parameters through the application of machine learning algorithms can result in better aeroelastic characteristics. Experimental validation of nonlinear phase and group velocities in terms of laser Doppler vibrometry on manufactured nano alumina/epoxy panels is necessary, alongside finite element analysis comparisons.

Author contributions Hamed Safarpour and Loke Kok Foong wrote the manuscript and prepared the figures. Murat Yaylacı reviewed the article and codding the mathematics formulation. Mustafa Bayram reviewed the article and codding the mathematics formulation.

Data availability The datasets used and/or analysed during the current study available from the corresponding author on reasonable request.

Declarations

Competing interests The authors declare no competing interests.

Open Access This article is licensed under a Creative Commons Attribution-NonCommercial-NoDerivatives 4.0 International License, which permits any non-commercial use, sharing, distribution and reproduction in any medium or format, as long as you give appropriate credit to the original author(s) and the source, provide a link to the Creative Commons licence, and indicate if you modified the licensed material. You do not have permission under this licence to share adapted material derived from this article or parts of it. The images or other third party material in this article are included in the article's Creative Commons licence, unless indicated otherwise in a credit line to the material. If material is not included in the article's Creative Commons licence and your intended use is not permitted by statutory regulation or exceeds the permitted use, you will need to obtain permission directly from the copyright holder. To view a copy of this licence, visit http://creativecommons.org/licenses/by-nc-nd/4.0/.

References

1. Liu, X. et al. 0000-0002-0005-9737, Dynamic Impact of Multi-Axle Trucks on Composite Girder Bridges with CSWs. *Int. J. Str. Stab. Dyn.* 2642020. https://doi.org/10.1142/S0219455426420204 (2026).
2. Nguyen, X. T., Hoang-Le, M., Khatir, S., Tran, M. T. & Cuong-Le, T. A New Modified Couple Stress Finite Element Model for Buckling Analysis of Laminated CNTs-Reinforced Composite Microplate. *Int. J. Str. Stab. Dyn.* 2650117. https://doi.org/10.1142/S0219455426501178 (2024).
3. Yan, J., Zhao, R., Sun, P. & Zhang, L. Aerodynamic Load Analysis and Fiber Orientation Optimization for Composite Blades. *Int. J. Str. Stab. Dyn.* 2750433. https://doi.org/10.1142/S0219455427504335 (2026).
4. Liu, Y. & Lu, J. F. Plane Wave Finite Element Method for the Dynamic Response of the Periodic Pile-Type Composite Ground Under a Harmonic Concentrated Load. *Int. J. Str. Stab. Dyn.* **26**, 2650043. https://doi.org/10.1142/S0219455426500434 (2026).
5. Anh, V. M., Quan, T. Q. & Tran, P. Nonlinear vibration and geometric optimization of nanocomposite multilayer organic solar cell under wind loading. *Thin-Walled Struct.* **158**, 107199 (2021).
6. Tounsi, A. et al. A Finite Element Approach for Forced Dynamical Responses of Porous FG Nanocomposite Beams Resting on Viscoelastic Foundations. *Int. J. Str. Stab. Dyn.* **26**, 2650078. https://doi.org/10.1142/S0219455426500781 (2026).
7. Allahkarami, F. & Tohidi, H. Size-dependent nonlinear free vibration of multilayer functionally graded graphene nanocomposite Timoshenko microbeam under different boundary conditions. *Eur. Phys. J. Plus*. **137**, 5 (2021).
8. Caliskan, U., Gulsen, H. & Apalak, M. K. New approach for modeling randomly distributed CNT reinforced polymer nanocomposite with van der Waals interactions. *Mech. Adv. Mater. Struct.* **31**, 218–229 (2024).
9. Chen, D., Yang, J. & Kitipornchai, S. Nonlinear vibration and postbuckling of functionally graded graphene reinforced porous nanocomposite beams. *Compos. Sci. Technol.* **142**, 235–245 (2017).
10. Bai, B. et al. A three-level discretization framework for dynamic behaviors of graphene-coated rotational blades with preset-angle sandwich structure under complex loads. *Sci. Rep.* (2026).
11. Guan, L., Tian, L., Hou, M. & Han, Y. Dynamics of a vibration-driven single disk. *Sci. Rep.* **11**, 16561 (2021).
12. Chen, J., Wu, J. & Chen, J. Control of stall flutter oscillations of a NACA0015 airfoil by attaching a porous plate. *Aerosp. Sci. Technol.* 110356. (2025).
13. Chang, L., Hu, Y. & Ragab, A. E. On the nonlinear wave propagations of improved solar cells. *Aerosp. Sci. Technol.* **146**, 108941 (2024).
14. Baghdasaryan, G. Y., Mikilyan, M. A., Vardanyan, I. A., Melikyan, K. V. & Marzocca, P. Thermoelastic non-linear flutter oscillations of rectangular plate. *J. Therm. Stresses*. **44**, 731–754 (2021).
15. Chen, X. et al. Three-dimensional oscillation characteristics in the bypass shock-induced thrust vector control. *Aerosp. Sci. Technol.* 111435. (2025).
16. Ding, H. X., Eltaher, M. & She, G. L. Nonlinear low-velocity impact of graphene platelets reinforced metal foams cylindrical shell: Effect of spinning motion and initial geometric imperfections. *Aerosp. Sci. Technol.* **140**, 108435 (2023).
17. Cao, Y., El-Meligy, M. & Garayev, M. Nonlinear Aerodynamic Flutter Responses of the Composite Pipes Conveying Two-Phase Flow Using Mathematical Simulation and Data-Driven Solution. *Aerosp. Sci. Technol.* 110947. (2025).
18. Duc, N. D., Seung-Eock, K., Tuan, N. D., Tran, P. & Khoa, N. D. New approach to study nonlinear dynamic response and vibration of sandwich composite cylindrical panels with auxetic honeycomb core layer. *Aerosp. Sci. Technol.* **70**, 396–404 (2017).
19. Fu, T., Wang, X. & Rabczuk, T. Broadband low-frequency sound insulation of stiffened sandwich PFGM doubly-curved shells with positive, negative and zero Poisson's ratio cellular cores. *Aerosp. Sci. Technol.* **147**, 109049 (2024).
20. Guo, W. et al. Robust adaptive dynamic programming for morphing air-breathing hypersonic vehicles under unmatched uncertainty. *Sci. China Inform. Sci.* **69**, 1–21 (2026).
21. Gao, H. et al. Turbulence correlation between moving trains and anemometer towers: Theoretical analysis, field measurements and simulation. *J. Wind Eng. Ind. Aerodyn.* **255**, 105949 (2024).
22. Feng, B. et al. Towards safe motion planning for industrial human-robot interaction: A co-evolution approach based on human digital twin and mixed reality. *Robot. Comput. Integr. Manuf.* **95**, 103012 (2025).
23. Nongyue, G., Changchuan, X., Chao, A., Zhiying, C. & Chen, S. Unified Aeroelastic and Flight Dynamics Formulation Based on State-Space Unsteady Aerodynamics. *AIAA J.* 1–18. (2026).
24. Xie, C., Zhu, L., An, C. & Shao, Y. A rapid steady/unsteady aerodynamic analysis method based on panel method coupled boundary layer theory. *Aerosp. Sci. Technol.* **165**, 110494 (2025).
25. Zhou, Y. et al. Droplet size and velocity distribution of a liquid jet in supersonic crossflow using LSD-PIV-based techniques. *Aerosp. Sci. Technol.* 112260. (2026).
26. Kang, H., Li, Z. M., Liu, T., Yuan, W. & Jing, J. Free vibration analysis of pre-twisted rotating dovetailed blade under the flexible connection with macro-micro rough contact topography. *Thin-Walled Struct.* **201**, 112039 (2024).
27. Kang, H., Li, Z. M., Liu, T., Mei, Q. & Zhang, X. Connection stiffness modeling of rotating dovetailed blade with macro-micro interface topography. *Eur. J. Mechanics-A/Solids*. **101**, 105064 (2023).

28. Wang, T., Zhu, Z., Zhou, X., Jing, T. & Chen, W. A function-based behavioral modeling method for air combat simulation. *J. Syst. Eng. Electron.* **35**, 945–954 (2024).
29. Xue, F. et al. Study on the influence of static terrain refinement correction on flow field simulation of Ulanqab wind power bases. *Renew. Energy* 125990. (2026).
30. Cheng, H., Song, L., Ouyang, Y., Zeng, F. & Guo, Z. Physics-enhanced performance prediction and intelligent design for wide-operating-range turbine blades. *Aerosp. Sci. Technol.* 112351. (2026).
31. Mao, J. et al. Wear-based time-variant reliability analysis on variable geometry turbine stator. *Aerosp. Sci. Technol.* 112016. (2026).
32. Ding, J., Bai, X., Zhao, W. & Xu, M. Orbit maintenance strategy integrated with power management for ultra low Earth orbit satellites. *Adv. Space Res.* (2026).
33. Wan, A. et al. Multiscale VMD-based deep learning with SHAP interpretability for offshore wind speed forecasting. *Electr. Power Syst. Res.* **261**, 113392 (2026).
34. Hou, Y., Sheng, Z., Song, Q., Ma, J. Z. & Wang, J. Flame Acceleration and Detonation Re-Initiation in Non-Premixed Rotating Detonation Engines. *AIAA J.* **64**, 2620–2633 (2026).
35. Cai, Z., Lin, X. & Liu, T. Physics-informed neural network for estimating surface heat flux from surface temperature measurements. *Int. J. Heat Mass Transf.* **253**, 127580 (2025).
36. Cai, Z., Fan, Z., Liu, T. & Kannaiyan, K. Neural network model for predicting aerodynamic parameters of airfoils. *J. Aircr.* **63**, 934–949 (2026).
37. Qiu, H. et al. Experimental investigation on enhancement method of flame diffusion width in a supersonic multi-strut fan-shaped annular combustor. *Appl. Therm. Eng.* 132077. (2026).
38. Zhu, M. et al. A Temperature-Humidity-Pressure Coupled Dynamic Model for Altitude Ground Test Facilities: From Component Modeling to System Validation. *Aerosp. Sci. Technol.* 113256. (2026).
39. Benjeddou, A. & Guerich, M. Free vibration of actual aircraft and spacecraft hexagonal honeycomb sandwich panels: a practical detailed FE approach. *Adv. Aircr. Spacecr. Sci.* **6**, 169 (2019).
40. Dastjerdi, S. et al. On the deformation and frequency analyses of SARS-CoV-2 at nanoscale. *Int. J. Eng. Sci.* **170**, 103604 (2022).
41. Dastjerdi, S., Akgöz, B. & Civalek, Ö. On the shell model for human eye in Glaucoma disease. *Int. J. Eng. Sci.* **158**, 103414. https://doi.org/10.1016/j.ijengsci.2020.103414 (2021).
42. Dastjerdi, S., Malikan, M., Eremeyev, V. A., Akgöz, B. & Civalek, Ö. Mechanical simulation of artificial gravity in torus-shaped and cylindrical spacecraft. *Acta Astronaut.* **179**, 330–344. https://doi.org/10.1016/j.actaastro.2020.11.005 (2021).
43. Dastjerdi, S., Malikan, M., Eremeyev, V. A., Akgöz, B. & Civalek, Ö. On the generalized model of shell structures with functional cross-sections. *Compos. Struct.* **272**, 114192. https://doi.org/10.1016/j.compstruct.2021.114192 (2021).
44. Dastjerdi, S., Alibakhshi, A., Akgöz, B. & Civalek, Ö. On a comprehensive analysis for mechanical problems of spherical structures. *Int. J. Eng. Sci.* **183**, 103796. https://doi.org/10.1016/j.ijengsci.2022.103796 (2023).
45. Dastjerdi, S., Civalek, Ö., Malikan, M. & Akgöz, B. On analysis of nanocomposite conical structures. *Int. J. Eng. Sci.* **191**, 103918. https://doi.org/10.1016/j.ijengsci.2023.103918 (2023).
46. Gao, W., Hu, J., Qin, Z. & Chu, F. Flexural wave manipulation in perforated metamaterial plates with acoustic black holes interconnected by piezoelectric studs. *Compos. Struct.* **321**, 117224 (2023).
47. Gao, W., Liu, Y., Qin, Z. & Chu, F. Wave propagation in smart sandwich plates with functionally graded nanocomposite porous core and piezoelectric layers in multi-physics environment. *Int. J. Appl. Mech.* **14**, 2250071 (2022).
48. Gao, W., Qin, Z. & Chu, F. Wave propagation in functionally graded porous plates reinforced with graphene platelets. *Aerosp. Sci. Technol.* **102**, 105860 (2020).
49. Kaushal, S., Zeeshan, M., Ansari, M. I. & Sharma, D. Progress in tribological research of Al2O3 ceramics: a review. *Mater. Today: Proc.* **82**, 163–167 (2023).
50. Koli, D. K., Agnihotri, G. & Purohit, R. A review on properties, behaviour and processing methods for Al-nano Al2O3 composites. *Procedia Mater. Sci.* **6**, 567–589 (2014).
51. Reddy, J. N. *Theory and analysis of elastic plates and shells* (CRC, 2006).
52. Fu, L., Huang, A., Gu, H. & Ni, H. Properties and microstructures of lightweight alumina containing different types of nano-alumina. *Ceram. Int.* **44**, 17885–17894 (2018).
53. Lamond, J. F. & Pielert, J. H. *Significance of tests and properties of concrete and concrete-making materials* (ASTM international, 2006).
54. Meiche, N. E., Tounsi, A., Ziane, N., Mechab, I. & Adda.Bedia, E. A. A new hyperbolic shear deformation theory for buckling and vibration of functionally graded sandwich plate. *Int. J. Mech. Sci.* **53**, 237–247. https://doi.org/10.1016/j.ijmecsci.2011.01.004 (2011).
55. Reddy, J. & Liu, C. A higher-order shear deformation theory of laminated elastic shells. *Int. J. Eng. Sci.* **23**, 319–330 (1985).
56. Cinefra, M., Moruzzi, M., Bagassi, S., Zappino, E. & Carrera, E. Vibro-acoustic analysis of composite plate-cavity systems via CUF finite elements. *Compos. Struct.* **259**, 113428 (2021).

57. Zeighampour, H., Tadi Beni, Y., Botshekanan, M. & Dehkordi Wave propagation in viscoelastic thin cylindrical nanoshell resting on a visco-Pasternak foundation based on nonlocal strain gradient theory. *Thin-Walled Struct.* **122**, 378–386. https://doi.org/10.1016/j.tws.2017.10.037 (2018).
58. Al-Furjan, M. S. H. et al. Energy absorption and vibration of smart auxetic FG porous curved conical panels resting on the frictional viscoelastic torsional substrate. *Mech. Syst. Signal Process.* **178**, 109269. https://doi.org/10.1016/j.ymssp.2022.109269 (2022).
59. Tahir, S. I. et al. An integral four-variable hyperbolic HSDT for the wave propagation investigation of a ceramic-metal FGM plate with various porosity distributions resting on a viscoelastic foundation. *Waves Random Complex. Media*. **34**, 1616–1639 (2024).

Publisher's note Springer Nature remains neutral with regard to jurisdictional claims in published maps and institutional affiliations.

Authors and Affiliations

Hamed Safarpour[1] · Loke Kok Foong[2,3] · Murat Yaylacı[4,5,6] · Mustafa Bayram[7]

✉ Hamed Safarpour
ha.safarpour@edu.ikiu.ac.ir

✉ Loke Kok Foong
lokekokfoong@duytan.edu.vn

1 Faculty of Engineering, Department of Mechanics, Imam Khomeini International University, Qazvin, Iran

2 Institute of Research and Development, Duy Tan University, Da Nang, Vietnam

3 School of Engineering & Technology, Duy Tan University, Da Nang, Vietnam

4 Department of Civil Engineering, Recep Tayyip Erdogan University, Rize 53100, Turkey

5 Dijitalpark Teknokent, Murat Yaylacı-Luzeri R&D Engineering Company, Rize 53100, Turkey

6 Turgut Kıran Maritime Faculty, Recep Tayyip Erdogan University, Rize 53900, Turkey

7 Department of Computer Engineering, Biruni University, Istanbul 34010, Turkey